

1991

# Characterization and analysis of the Bulk-Acoustic-Wave Thin Film Resonator in sub-nanogram mass detection

Ronald Patrick O'Toole  
*Iowa State University*

Follow this and additional works at: <https://lib.dr.iastate.edu/rtd>

 Part of the [Acoustics, Dynamics, and Controls Commons](#), and the [Signal Processing Commons](#)

## Recommended Citation

O'Toole, Ronald Patrick, "Characterization and analysis of the Bulk-Acoustic-Wave Thin Film Resonator in sub-nanogram mass detection" (1991). *Retrospective Theses and Dissertations*. 16963.  
<https://lib.dr.iastate.edu/rtd/16963>

This Thesis is brought to you for free and open access by the Iowa State University Capstones, Theses and Dissertations at Iowa State University Digital Repository. It has been accepted for inclusion in Retrospective Theses and Dissertations by an authorized administrator of Iowa State University Digital Repository. For more information, please contact [digirep@iastate.edu](mailto:digirep@iastate.edu).

**Characterization and analysis  
of the Bulk-Acoustic-Wave Thin Film Resonator  
in sub-nanogram mass detection**

**by**

**Ronald Patrick O'Toole**

**A Thesis Submitted to the  
Graduate Faculty in Partial Fulfillment of the  
Requirements for the Degree of  
MASTER OF SCIENCE**

**Department: Electrical Engineering and Computer Engineering  
Major: Electrical Engineering**

Signatures have been redacted for privacy

**Iowa State University  
Ames, Iowa**

**1991**

## TABLE OF CONTENTS

	Page
1. INTRODUCTION	1
1.1. Statement of Purpose	1
1.2. Overview	2
2. THIN FILM RESONATOR OPERATION	4
2.1. Piezoelectric Resonator Operation	4
2.2. Equivalent Circuit Model	9
2.3. Electrical Modelling Parameters	15
2.4. Thin Film Resonator Analysis	25
2.5. Resonator Measurement and Modelling	28
3. MASS DETECTION ANALYSIS	41
3.1. Mass Loading Resonator Analysis	41
3.2. Parasitic Frequency Effects	47
3.3. Thin Film Coatings	59
4. TFR MASS LOADING RESULTS	64
4.1. Photoresist Thin Film Coatings	64
4.2. PMMA Thin Film Coatings	75
5. SUMMARY AND RECOMMENDATIONS	83
BIBLIOGRAPHY	85
ACKNOWLEDGEMENTS	89

	Page
APPENDIX A: O'TOOLE, R. P., BURNS, S. G., SHANKS, H. R., D'SILVA, A., AND PORTER, M. D. "MICROWAVE FREQUENCY OSCILLATORS BASED ON ALN: TOWARD INTEGRATED CHEMICAL SENSORS." PRESENTED AT ELECTROCHEMICAL SOCIETY SYMPOSIUM, SEATTLE, WASHINGTON, OCTOBER 1990.	90
APPENDIX B: MAXIMUM IMPEDANCE PHASE FREQUENCY DERIVATION	92
APPENDIX C: IMPEDANCE MAGNITUDE MAXIMUM AND MINIMUM FREQUENCY DERIVATION	95
APPENDIX D: LIBRA SIMULATION FILE	99

## INTRODUCTION

### 1.1. Statement of Purpose

The unique attributes from the standpoint of size and high frequency performance of the Thin Film Resonator (TFR) are numerous. However, the fundamental utility of TFR technology has been in its ability to be fabricated on a silicon substrate and thus allow complete microelectronic integration with active devices. The past and present research of TFR technology in high frequency applications have mostly comprised of oscillator and filter design. Pierce oscillators using the TFR as the frequency control element has already been designed in both hybrid [1,2] and integrated form [3]. The use of TFR technology in microwave filter design as a feedback element in resonators operating at 1 GHz has also been investigated in both monolithic and stacked crystal filter (SCF) topologies [4,5]. However, the unique ability of the TFR to be used in miniaturized microbalance applications for chemical sensing has just previously been shown to possess great potential [6]. Appendix A contains an abstract of this initial study which was presented at the Electrochemical Society conference in October, 1990.

The purpose of this research work is to investigate and characterize the mass-sensing properties of the TFR in its present technology. The initial proof of concept for which the resonant frequency shift effect due to the added acoustic cavity will be shown. From this, the ability of the TFR to perform as an extremely sensitive chemical sensor will be investigated which provides interesting information on the physical properties of the deposited organic film used to separate or extract the gas phase analyte. For this initial study, the gas

phase analyte which will be detected is methanol. The thin films used to sense the methanol will be photoresist and poly (methyl methacrylate) (PMMA).

## 1.2. Overview

Chapter 2 describes the operation of the bulk-acoustic-wave thin-film resonator. Initially, a generalized description of the piezoelectric effect will be given from which the material properties of the piezoelectric film will be analyzed. This analysis leads to the possibility of modelling the one-dimensional bulk-acoustic resonator as an equivalent circuit in the Butterworth - Van Dyke format. The impedance of the equivalent circuit near resonance provides numerous points of interest which depend on varying degrees on the circuit components. Thus, the characterization of the equivalent circuit model and its impedance behavior near resonance is analyzed to understand the effects of the resonant frequency shift effect on the circuit parameters. The topology of the TFR as it exists in this study is also presented which details its attributes and limitations. Finally, the data extraction technique and preliminary modelling will be given which will investigate the possibility of further modelling parasitics.

Chapter 3 examines the TFR as an acoustic cavity from which the relationship between the physical topology and resonant frequency will be shown in a one-dimensional model. This analysis provides the theory and limitations on the mass sensitivity of the TFR. The parasitic frequency effects of the TFR are also investigated from which the resonant pattern will be analyzed by varying the impedance parameters. Finally, the last section describes the

thin coatings used in this analysis which will be used to verify the mass sensitivity and minimum detectable mass of the TFR.

Chapter 4 analyzes the mass-loading frequency-shift mechanism by calculating the motional impedance parameters using the EIA-512 standard [10]. These preliminary data illustrate the resonant frequency shift of the coated TFR when exposed to the methanol analyte over an extended period of time and tries to show a relationship between the mass loading and the motional impedance parameter changes. Chapter 5 contains the summary and suggestions for future work.

Appendix A contains the abstract of the presentation given at the Electrochemical Society symposium in October, 1990, which described the utility of the TFR as a sensitive chemical sensor. Appendix B contains the detailed derivation of the maximum impedance phase frequency for the TFR model. The detailed derivation of the impedance magnitude maximum frequency and impedance magnitude minimum frequency is given in Appendix C. Appendix D is a representative Libra<sup>TM</sup> simulation file used to extract the TFR electrical model circuit parameters.

## 2. THIN FILM RESONATOR OPERATION

### 2.1. Piezoelectric Resonator Operation

Piezoelectric crystals have long been used to control and manage the frequencies in electrical communication. The most notable piezoelectric crystal is the quartz crystal which is used extensively due to its accuracy, cost, reliability, and convenience. The ability of the quartz crystal to provide frequency control lies in its coupling between the mechanical resonance frequency of the piezoid and the associated electric field, i.e., it is an electromechanical transducer. This characteristic is termed *piezoelectricity* which literally means "pressure electricity". The definition which is most generally used to describe piezoelectricity is as follows [7] : "piezoelectricity is electric polarization produced by mechanical strain in crystals belonging to certain classes, the polarization being proportional to the strain and changing direction with it." [p. 2] The production of electric polarization by application of a strain in the crystal is the direct piezoelectric effect. Conversely, the application of a polarizing electric field to the crystal may cause the crystal to experience a mechanical strain in its bulk which is termed the converse piezoelectric effect. The electromechanical coupling and stresses associated with the applied electric field depend upon the crystal symmetry and the placement of the electrode contacts used to apply the electric field. The various modes of electromechanical coupling result in different acoustic waves, modes of propagation, and particle displacement. This is best illustrated by noting the various modes which can be excited in certain crystal piezoids: thickness

shear, face shear, longitudinal, surface acoustic wave (SAW), shear horizontal, and flexural modes.

In order to physically understand the piezoelectric effect, consider a symmetric distribution of point charges in a hexagonal fashion as shown in Figure 2-1. The crystal can be considered to consist of ions arranged like the charges of Figure 2-1. The x-axis is taken to be parallel to the

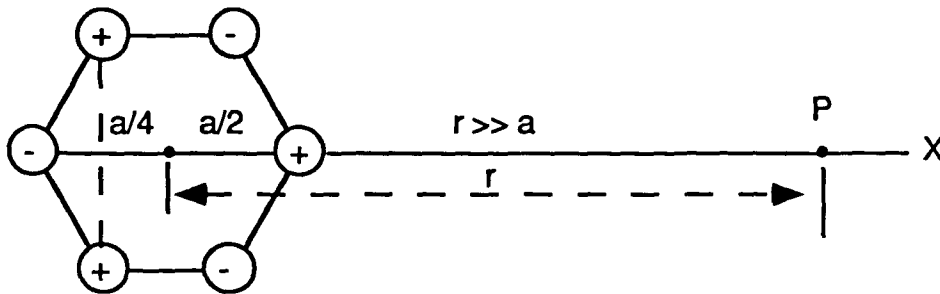


Figure 2-1. Two dimensional orientation of electric charges

line joining opposite charges and  $a$  is the distance between the charges along this line. The potential  $V$  at the point  $P$  at a distance  $r$  where  $r \gg a$  for the three positive charges can be computed to be :

$$V_+ = 4\pi\epsilon_0 \left( \frac{q}{r-a/2} + \frac{2q}{r+a/4} \right) \approx 4\pi\epsilon_0 \frac{3q}{r} \quad (2.1)$$

which is the potential at point  $P$  due to a charge of  $+3q$  located at a distance  $r$ . However, the total potential at  $P$  is zero due to the negative potential contribution of the three negative charges.

A force is then applied along the  $Y$ -axis to the hexagonal crystal structure as shown in Figure 2-2 causing the system of charges to be distorted. Now, the

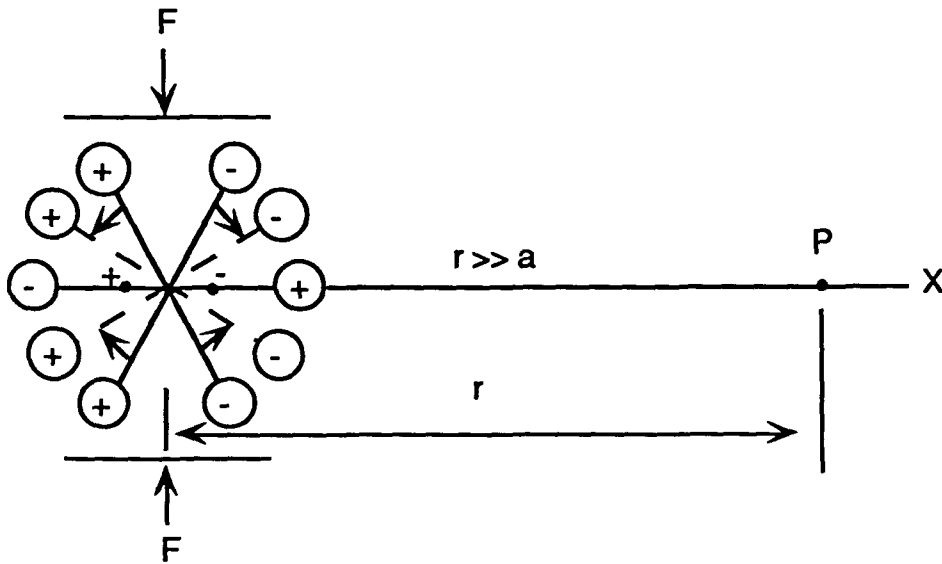


Figure 2-2. The effects of compressional strain

center of gravity of the positive charges has moved to the left while the center of gravity of the three negative charges moves to the right. The result is that a dipole moment has been created with respect to point P. A potential also exists at point P and thus an electric field has been created ( $E = -dV/dr$ ) due to the application of the force in the Y-direction. The dipole moment per unit volume, the polarization  $P$ , experienced within this crystal can be related to the induced strain by:

$$P = \epsilon x \quad (2.2)$$

where  $P$  is the polarization,  $x$  the strain, and  $\epsilon$  is the piezoelectric coefficient (not related to the permittivity of free space  $\epsilon_0$ ). Thus, it is also conversely true that a piezoelectric crystal placed in an electric field may experience one or

more kinds of mechanical strain. The strain is proportional to the applied field and is written as:

$$x = d E \quad (2.3)$$

where  $x$  is the strain,  $E$  is the alternating electric field, and  $d$  is the piezoelectric strain coefficient. In an electric field, positive and negative ions tend to be driven in opposite directions and a dipole tends to rotate to align itself with the direction of the field. The resulting displacements produce strains on the crystal lattice which are known as the converse piezoelectric effect. This causes a vibrational or oscillatory motion in the crystal resulting in the generation of acoustic standing waves. Due to the crystal structure, i.e. angle of cut, crystal structure and thickness, there exists a strong preference to vibrate at a characteristic resonant frequency. At this characteristic resonant frequency, resonator impedance analysis reveals sharp impedance magnitude and phase changes over a relatively small frequency range indicative of a high quality factor,  $Q$ . The quality factor  $Q$  is defined in many fashions but is most generally described as the ratio of energy stored to the energy dissipated per cycle. A high quality factor piezoid resonates with minimal energy dissipation.

The operation of a piezoid resonator in mass detection is a complicated function of the acoustic impedances of the various layers, where each layer is expressed in terms of its thickness, mass density, effective elastic constants, and viscosity resulting in a complex transfer matrix solution. However a physical description of the mass detection is best explained in terms of the thickness-shear mode exhibited by an AT-cut quartz crystal resonator [8]. This resonator is configured such that an electric field applied between the excitation

electrodes results in a shear mode of vibration of the quartz crystal analogous to transverse waves on a string of length  $L$  bound at both ends where the standing waves have wavelengths of integral divisors of  $2L$ . The string resonates when it is pulsed at a frequency characteristic of the fundamental resonant frequency or one of its harmonics. The fundamental frequency of the string is given by:

$$f_0 = \left(\frac{S}{m_L}\right)^{1/2} \frac{1}{2L} \quad (2.4)$$

where  $S$  is the tension on the string and  $m_L$  is the mass per unit length. An increase in  $m_L$  decreases the resonant frequency which corresponds to an increase in mass on one of the crystal resonator excitation electrodes.

Furthermore, an increase in  $L$  also decreases the resonant frequency as illustrated in equation (2.4). This is analogous to the deposition of a thin film on the electrode surface since the acoustic waves of the resonator travel through this material also. For the case of the shear mode of the AT-cut quartz crystals, the fundamental shear mode resonance has been explicitly quantified and is given by:

$$f_0 = \left(\frac{\mu}{\rho}\right)^{1/2} \frac{1}{2t_q} \quad (2.5)$$

where  $\mu$  is the shear modulus,  $\rho$  is the density, and  $t_q$  is the thickness between the electrode contacts. Increasing the density or thickness of the quartz crystal results in a decrease of the fundamental resonant frequency corresponding to the string example.

The most fundamental relation between frequency-shift and mass-loading due to interfacial mass changes of a thickness shear-mode crystal was first formulated by Sauerbrey [9] :

$$\Delta f = - \left( \frac{2 f_q^2}{\rho_q v_q A} \right) \Delta m_f \quad (2.6)$$

where  $\Delta f$  is the resonant frequency shift,  $\Delta m_f$  is the change in mass,  $f_q$  the fundamental resonant frequency before the added mass,  $A$  the active area,  $v_q$  the acoustic phase velocity, and  $\rho_q$  the density of the crystal. Equation (2.6) shows that the crystal resonator is sensitive to mass changes per unit area of oscillation and appears to be independent of all other properties of the deposited thin film. However, the Sauerbrey relation is an first order approximation and is only rigorously appropriate for infinitesimally thin films that have acoustic impedances identical to that of the piezoelectric material. In practice, the Sauerbrey relation is valid up to loadings approaching 10% of the crystal mass [8].

## 2.2. Equivalent Circuit Model

A crystal resonator in its simplest form consists of a piezoelectric film or crystal with electrodes attached in such a fashion as to excite one of its resonant frequencies when a voltage is applied across its terminals. The complex impedance of the resonator is found using Ohm's law by applying a voltage and measuring the current displaced through the crystal. The electrical behavior of this resonator, as evidenced by the complex impedance, over a narrow range

of frequencies near a resonance can be modeled by an equivalent circuit. When the resonant mode of interest is sufficiently isolated from other modes of motion, the parameters of the equivalent circuit may be considered to be independent of frequency, and the equivalency will be nearly exact over a frequency band of at least a few percent [10].

The standard equivalent circuit used to model the electrical behavior of piezoelectric resonators is the Butterworth - Van Dyke equivalent circuit given in Figure 2-3. The four circuit elements consist of the motional parameters: R (motional resistance), L (motional inductance), and C (motional capacitance); and the static capacitance  $C_0$ . The static capacitance,  $C_0$ , is the analogous

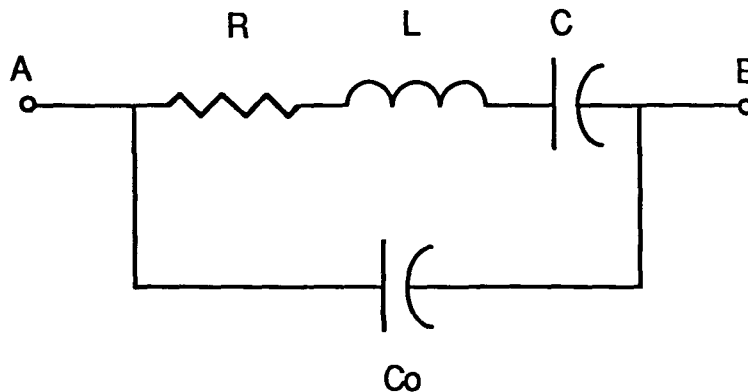


Figure 2-3. Butterworth - Van Dyke equivalent circuit model for the piezoelectric resonator

parallel plate capacitance seen between the electrode contacts where in its simplest form can be represented by equation (2.7):

$$C_0 = \frac{\epsilon_0 \epsilon_r A}{t} \quad (2.7)$$

where  $\epsilon_0$ ,  $\epsilon_r$  are the permittivity of free space and the relative permittivity, respectively,  $A$  is the electrode area, and  $t$  is the thickness of the piezoelectric dielectric. Equation (2.7) is only valid for a realizable geometric area and a thin piezoelectric layer (no fringing assumption).

The motional parameters:  $R$ ,  $L$ , and  $C$ , are much more difficult to theoretically compute since they depend upon the piezoelectric effect for the coupling between the mechanical strain in the resonator and the applied electric field. Bottom [7] presents a simplified approach to this effect where he derives the expressions for the parameters of the equivalent circuit. The analysis begins by solving the one dimensional equation of motion, equation (2.8 ),

$$\rho \frac{\partial^2 \psi}{\partial t^2} - c \frac{\partial^2 \psi}{\partial y^2} + r \frac{\partial \psi}{\partial t} = 0 \quad (2.8)$$

assuming the damping forces are proportional to the particle velocity. In equation (2.8),  $\psi$  is the particle displacement,  $\rho$  is the density of the piezoelectric material,  $c$  is the appropriate elastic constant, and  $r$  is the damping coefficient. The elastic constant,  $c$ , is a proportionality constant in the stress - strain relationship in matrix form as shown in equation (2.9)

$$-[X] = [c] [x] \quad (2.9)$$

where  $[X]$  are the extensional and shear stress components and  $[x]$  are the extensional and shear strain components. Assuming a solution of the form:

$$\psi = A(y)\exp(j\omega t) \quad (2.10)$$

and applying the boundary conditions: 1)  $\psi=0$  at the center of the plate where  $y=0$ ; and 2) the stress at the surface,  $y=e/2$ , is due to the applied electric field alone; the particle displacement wave can be found using equation (2.3) in terms of the applied voltage  $V_m \exp(j\omega t)$ :

$$\psi = \frac{d V_m}{\gamma e \cos\left(\frac{\gamma e}{2}\right)} \sin(\gamma y) \exp(j\omega t) \quad (2.11)$$

where  $\gamma$  is the complex quantity:

$$\gamma = \left[ \frac{\omega^2}{v^2} - \frac{j\omega r}{\rho v^2} \right]^{1/2} \quad (2.12)$$

and  $v$  is the wave velocity  $(c/\rho)^{1/2}$ . The strain can be found by differentiating the particle displacement equation with respect to the displacement direction from which the polarization can be calculated by multiplying the strain by the appropriate piezoelectric constant (reference equation 2.2). The space charge density is next found by taking the negative of the gradient of the polarization :

$$q_v(y) = - \frac{\partial P_y}{\partial y} \quad (2.13)$$

where  $q_v(y)$  is the space charge density. Poisson's equation in one dimension:

$$\frac{\partial^2 V}{\partial y^2} = -\frac{q_v(y)}{k \epsilon_0} \quad (2.14)$$

is used to obtain the potential by integrating twice throughout the plate via the applied potential where  $\epsilon_0$  is the permittivity of free space and  $k$  is the relative dielectric constant of the piezoelectric crystal. The gradient relationship in one dimension:

$$E = -\frac{\partial V}{\partial y} \quad (2.15)$$

is next applied to find the electric field intensity throughout the piezoelectric crystal. Since the piezoelectric material is assumed to be a dielectric, the conduction current density is zero and thus the current density at the surface is composed of displacement current:

$$j_s = k \epsilon_0 \frac{\partial E}{\partial t} \quad (2.16)$$

Finally, the electric admittance of the piezoelectric resonator can be obtained by dividing equation (2.16) by the applied voltage. After considerable mathematical manipulation and approximations, the four circuit elements can be extracted from the admittance equation as a function of the properties of the piezoelectric material [7]:

$$R = \frac{e^3 r}{8 A \epsilon^2}$$

$$L = \frac{e^3 \rho}{8 A \epsilon^2}$$

$$C = \frac{8 A \epsilon^2}{e c \pi^2}$$

$$C_0 = \frac{k \epsilon_0 A}{e} \quad (2.17).$$

The two geometrical properties found in the above equation are the thickness  $e$  and the electrode area  $A$ . The piezoelectric stress coefficient,  $\epsilon$ , as defined in equation (2.2) is responsible for the existence of the motional parameters since it appears in each of the three definitions. Note that  $C_0$  does not depend on the piezoelectric effect since  $\epsilon$  does not appear in its equation.

The extraction of the three motional parameters from the equation of motion of the piezoelectric crystal appears to verify the existence of the Butterworth - Van Dyke equivalent circuit model since the admittance expressed in terms of the properties of the piezoelectric crystal simulate a series RLC circuit. However, the assumptions used in the derivation should be carefully considered before drawing any absolute conclusions. In the derivation, the piezoid is considered to be an infinitely large, thin plate with the displacement wave traveling in the thickness direction and thus the problem is one dimensional. Implicit in this assumption is that a single mode of vibration exists with no other coupling to other modes and the displacement wave is constant in the plane parallel to the electrode surface. For these assumptions to hold, a perfectly symmetrical crystal lattice is necessary, a requirement which is very difficult to attain. Even in quartz, the ability to obtain a pure crystalline sample cut at the correct angle is very difficult. Thus, in reality, there are usually

parasitic modes which are excited simultaneously and thus some input energy is coupled off to these modes. It is also not possible to compute  $R$  since the value of the damping coefficient,  $r$ , cannot be directly measured or calculated. In the derivation,  $r$  is assumed to include all dissipative forces which are proportional to the particle velocity in the piezoid. There are other sources of damping which are present such as the coupling of the acoustic wave to the air or material covering the electrode, internal dissipation, surface friction, and mounting losses.

Despite the semi - quantitative nature of the expressions for the motional parameters, important physical information can be deduced from equation (2.17). The motional resistance,  $R$ , represents the dissipation of electrical energy in the piezoid material. Some of the electrical energy is converted to thermal energy in the piezoid while some of the energy in the form of acoustic waves gets coupled to the surrounding medium, damped on the electrode surface, or gets coupled into parasitic modes.

The motional inductance,  $L$ , is directly proportional to the density of the piezoid and is thus generally related to the mass including the coating on its electrode surface. Also, the inductance is inversely related to the area and thus it can be physically altered. The motional capacitance,  $C$ , contains the elastic constant,  $c$ , and thus represents the elastic properties of the piezoid.

### **2.3. Electrical Modelling Parameters**

In the previous section, the equivalent circuit model for the piezoelectric resonator was shown to be the Butterworth - Van Dyke circuit model as illustrated in Figure 2-3. In order to accurately characterize the impedance

behavior of the piezoelectric resonator, theoretical expressions describing the various characteristics near resonance are necessary. Figure 2-4 illustrates a representative impedance magnitude and phase plot of a thin film resonator where the frequency span completely covers the fundamental resonance range. The vertical axis to the left which ranges from -90 to +90 degrees is the impedance phase in degrees while the right vertical axis which ranges from 0 to 300 is the linear impedance magnitude in ohms. The frequency is plotted along the horizontal scale in GHz. Included in Figure 2-4 are the various features which will be investigated in order to thoroughly and accurately characterize the resonant behavior.

The impedance  $Z_{AB}$  between the terminals A and B of Figure 2-3 is given by:

$$Z_{AB} = \frac{\left(j\omega L + \frac{1}{j\omega C} + R\right) \left(\frac{1}{j\omega C_0}\right)}{j\omega L + \frac{1}{j\omega C} + R + \frac{1}{j\omega C_0}} \quad (2.18)$$

Multiplying the numerator and denominator by the complex conjugate of the denominator and simplifying results in:

$$Z_{AB} = (A1 - jB1)/C1 \quad (2.19)$$

where

$$A1 = R \left( \frac{L}{C_0} - \frac{1}{\omega^2 C C_0} \right) - \left( \frac{R}{\omega C_0} \right) \left( \omega L - \frac{1}{\omega C} - \frac{1}{\omega C_0} \right)$$

$$B1 = \left( \frac{L}{C_0} - \frac{1}{\omega^2 C C_0} \right) \left( \omega L - \frac{1}{\omega C} - \frac{1}{\omega C_0} \right) + \frac{R^2}{\omega C_0}$$

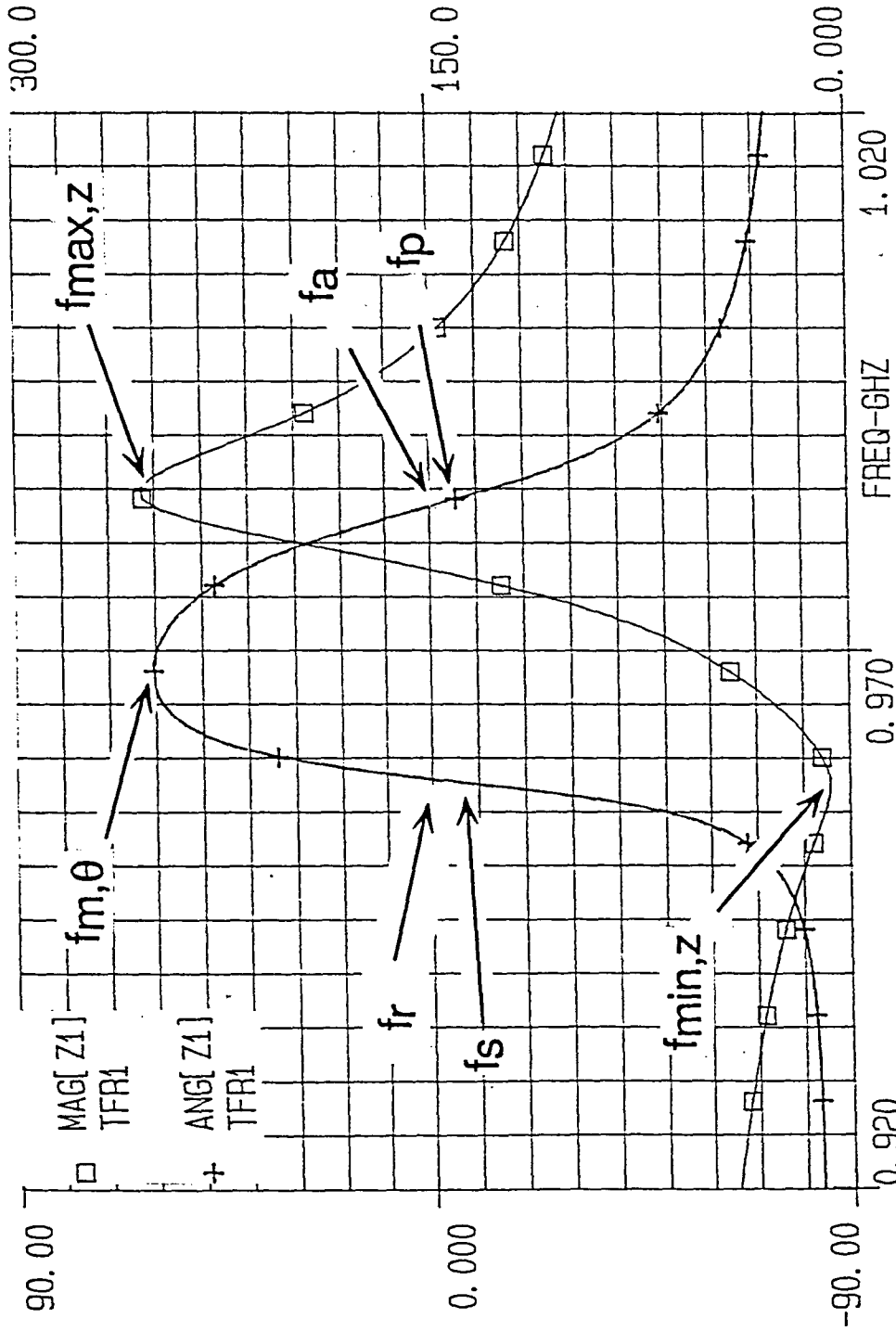


Figure 2-4. Impedance magnitude and phase of TFR

and

$$C1 = R^2 + \left( \omega L - \frac{1}{\omega C} - \frac{1}{\omega C_0} \right)^2$$

For the circuit to be resonant, the imaginary part of equation (2.19) should be equal to zero. Thus setting B1, the imaginary part of equation (2.19) , equal to zero and multiplying out the terms results in:

$$\left( \frac{\omega L^2}{C_0} - \frac{2L}{\omega C C_0} - \frac{L}{\omega C_0^2} + \frac{1}{\omega^3 C^2 C_0} + \frac{1}{\omega^3 C_0^2 C} + \frac{R^2}{\omega C_0} \right) = 0 \quad (2.20)$$

Equation (2.20) can be simplified by clearing fractions resulting in a fourth order equation:

$$\omega^4 C^2 L^2 C_0 - 2\omega^2 C C_0 L - \omega^2 C^2 L + \omega^2 R^2 C^2 C_0 + C + C_0 = 0 \quad (2.21)$$

The two zero phase resonant frequencies  $f_r$ , the lower resonant frequency, and  $f_a$ , the anti-resonant or upper resonant frequency, can be solved from equation (2.21) to yield:

$$f_r = \frac{\sqrt{2}}{4\pi} \sqrt{\frac{2}{CL} + \frac{1}{C_0 L} - \frac{R^2}{L^2} - \sqrt{\frac{\left(-\frac{2}{C} - \frac{1}{C_0} + \frac{R^2}{L}\right)^2}{L^2} - \frac{4\left(\frac{1}{C} + \frac{1}{C_0}\right)}{CL^2}}} \quad (2.22)$$

$$f_a = \frac{\sqrt{2}}{4\pi} \sqrt{\frac{2}{CL} + \frac{1}{C_0 L} - \frac{R^2}{L^2} + \sqrt{\frac{\left(-\frac{2}{C} - \frac{1}{C_0} + \frac{R^2}{L}\right)^2}{L^2} - \frac{4\left(\frac{1}{C} + \frac{1}{C_0}\right)}{CL^2}}} \quad (2.23)$$

Equations (2.22) and (2.23) are the true resonant frequencies of the Butterworth - Van Dyke equivalent circuit used to model the resonator. However, certain simplifications can be made to  $f_r$  and  $f_a$  which results in the more general and standard resonant frequencies  $f_s$  and  $f_p$ . Considering the quantity inside the inner square root:

$$\sqrt{\frac{4\left(\frac{-1}{C} - \frac{1}{2C_0} + \frac{R^2}{2L}\right)^2}{L^2} - \frac{4\left(\frac{1}{C} + \frac{1}{C_0}\right)}{CL^2}} \quad (2.24)$$

which can be multiplied out and reduced to:

$$\sqrt{4\left(\frac{R^2}{2L^2} - \frac{1}{2LC_0}\right)^2 - \frac{4R^2}{L^3C}} \quad (2.25)$$

However, simplifications can be made to equation (2.25) since for most practical resonators:

$$4\left(\frac{R^2}{2L^2} - \frac{1}{2LC_0}\right)^2 \gg \frac{4R^2}{L^3C} \quad (2.26)$$

Thus, when equation (2.26) is substituted in equation (2.22) for the term inside the inner square root, the equation simplifies down to the familiar series resonant frequency:

$$f_s = \frac{1}{2\pi} \frac{1}{\sqrt{LC}} \quad (2.27)$$

while the same substitution into equation (2.23) results in:

$$f_p = \frac{1}{2\pi} \sqrt{\frac{1}{LC} + \frac{1}{LCo} - \frac{R^2}{L^2}} \quad (2.28)$$

However, further simplifications can be made to equation (2.28) since :

$$\frac{1}{LC} + \frac{1}{LCo} \gg \frac{R^2}{L^2} \quad (2.29)$$

Therefore, the final expression for the parallel resonant frequency is given as:

$$f_p = \frac{1}{2\pi} \sqrt{\frac{1}{LC} + \frac{1}{LCo}} \quad (2.30)$$

In evaluating the resonant frequency shift of a resonator due to various load capacitances or added mass, the accuracy necessary to evaluate the frequency sensitivity of the resonator requires that equations (2.22) and (2.23) be utilized to calculate the most accurate solution. In general, the expressions for  $f_s$  and  $f_p$  are utilized for oscillator design and quick calculations for most practical situations.

By definition, the impedances at  $f_r$  and  $f_a$  are purely real. The resonant frequency,  $f_r$ , is commonly referred to as the frequency of zero phase, minimum impedance point while the anti-resonant frequency,  $f_a$ , is referred to as the frequency of zero phase, maximum impedance point. Thus, expressions for these impedances can be found by substituting equations (2.22) and (2.23) into the impedance expression (2.19):

$$Z_{\omega r} = \frac{2 R L}{\left( L + R^2 C_0 + L^2 C_0 \sqrt{\frac{\left( \frac{-2}{C} - \frac{1}{C_0} + \frac{R^2}{L} \right)^2}{L^2} - \frac{4 \left( \frac{1}{C} + \frac{1}{C_0} \right)}{C L^2}} \right)} \quad (2.31)$$

for the impedance at the zero - phase resonant frequency and

$$Z_{\omega a} = \frac{2 R L}{\left( L + R^2 C_0 - L^2 C_0 \sqrt{\frac{\left( \frac{-2}{C} - \frac{1}{C_0} + \frac{R^2}{L} \right)^2}{L^2} - \frac{4 \left( \frac{1}{C} + \frac{1}{C_0} \right)}{C L^2}} \right)} \quad (2.32)$$

for the impedance at the zero-phase anti-resonant frequency. Unfortunately, the resulting equations are lengthy and complex from which very little practical information can be extracted. However, if the equations for the series and parallel resonant frequencies are substituted into the impedance expression, equation (2.19), and the imaginary terms are ignored for the purpose of clarity, the approximate real impedance expressions can be found for the zero - phase frequencies:

$$Z_{\omega s} = \frac{R L C}{C L + R^2 C_0^2} \quad (2.33)$$

for the impedance at series resonance and

$$Z_{\omega p} = \frac{C L}{C_0(C + C_0)R} \quad (2.34)$$

for the impedance at parallel resonance.

Under certain circumstances, the impedance phase during resonance does not get above zero. The resonant and anti-resonant frequencies,  $f_r$  and  $f_a$ , cease to exist when the maximum phase doesn't cross the  $\theta=0$  line on Figure 2-4. However, the maximum phase still exists and is available for determining any relative frequency shift due to a change in the loading environment. The derived equation for  $f_{m\theta}$ , the maximum impedance phase, is found by taking the derivative of the impedance phase with respect to frequency and solving for the frequency which results in:

$$f_{m\theta} = \frac{1}{2\pi\sqrt{6}} \sqrt{E2 + E1} \quad (2.35)$$

where

$$E1 = \sqrt{12 \left(1 + \frac{C}{C_0}\right) + \left(C^2 R^2 \omega_s^2 - \frac{C}{C_0} - 2\right)^2}$$

and

$$E2 = 2 + \frac{C}{C_0} - C^2 R^2 \omega_s^2$$

The complete derivation of equation (2.35) can be found in Appendix B.

The frequency of the impedance magnitude extremes are another set of points which are used to detect relative frequency shifts under the conditions of changing impedance magnitude and phase which is generally done in thin film coating studies. The impedance magnitude of the piezoelectric resonator has one minimum,  $f_{min,z}$ , and one maximum,  $f_{max,z}$ , which are given as:

$$f_{\min,z} = f_s \left( \frac{1}{1 + \frac{C_0 R^2}{2L}} \right) \quad (2.36)$$

$$f_{\max,z} = f_s \left( \frac{4 C_0 L + 2 C L - C C_0 R^2}{4 C_0 L - 2 C_0^2 R^2} \right) \quad (2.37)$$

The minimum and maximum impedance magnitude frequencies are found by calculating the derivative of the impedance magnitude with respect to frequency and solving for the two root frequencies. The complete derivation of equations (2.36) and (2.37) are given in Appendix C.

One of the properties used to characterize piezoelectric resonators as a frequency control element is the quality factor or Q. In general, the Q of any resonant system is given by:

$$Q = 2\pi \frac{\text{Maximum energy stored}}{\text{Total Energy dissipated per cycle}}$$

Thus, Q is a figure of merit which is inversely proportional to the dissipation of energy in the resonant cavity. There are various causes that lead to a low Q, the most probable being:

- (1) Intrinsic acoustic losses in the body of the material which are caused by the basic material parameters and processing defects.
- (2) Acoustic loss at the surface of the resonator due to the coupling to the surrounding medium or to a "lossy" viscous coating.
- (3) Energy loss in the electrode material due to the type of material being used as well as any defects owing to poor metallization.

- (4) Electrical losses due to mounting the resonator such as parasitic capacitances and inductances.

For a circuit which is intended to be frequency selective, the quality of the circuit is measured by the sharpness of the selectivity. This is best exemplified by the following equation for Q:

$$Q = \frac{\omega}{\omega^2 L C + 1} \frac{\partial \theta}{\partial \omega} \Big|_{\omega = \omega_s, \omega_p} \quad (2.38)$$

$$= \frac{C + C_0 + C^2 L \omega^2 + 2 C C_0 L \omega^2 - C^2 C_0 R^2 \omega^2 - 3 C^2 C_0 L^2 \omega^4}{C^2 R \omega (1 + C L \omega^2)} \Big|_{\omega = \omega_s, \omega_p} \quad (2.39)$$

where  $\theta$  is the impedance phase. This illustrates that Q is directly proportional to the change of the impedance phase with respect to frequency or the "phase slope" evaluated at the series or parallel resonant frequency. Equation (2.38) is derived by finding the impedance phase of a series RLC circuit and approximating the phase near zero:

$$\theta = \tan^{-1} \left( \frac{\omega L - \frac{1}{\omega C}}{R} \right) \approx \left( \frac{\omega L - \frac{1}{\omega C}}{R} \right) \quad (2.40)$$

The derivative of  $\theta$  with respect to  $\omega$  is then taken and Q for the series resonant frequency case is substituted in:

$$Q = \frac{1}{\omega R C} \quad (2.41)$$

which simplifies to equation (2.38). The Q calculation for the resonator equivalent circuit is not simply the series resonant case due to the coupling effect of the parallel capacitor  $C_0$ . However, the value of Q for the series resonance of the resonator model should be similar to the theoretical expression given in equation (2.41). The resulting expression for the series resonant Q of the resonator model is:

$$Q \Big|_{\omega=\omega_s} = \frac{2L - C_0 R^2}{2R \sqrt{LC}} \quad (2.42)$$

Since  $2L \gg C_0 R^2$  for most practical resonators, equation (2.42) simplifies down to equation (2.41). The Q calculation for the parallel resonant case is done in the same fashion except that the C in equation (2.38) is replaced by the series combination of the motional capacitance C and the body capacitance  $C_0$  and the equation is evaluated at the parallel resonant frequency:

$$Q \Big|_{\omega=\omega_p} = \frac{\sqrt{\frac{1}{LC_0} + \frac{1}{LC}} (2L + R^2 C_0)}{2R} \approx \frac{\omega_p L}{R} \quad (2.43)$$

which also reduces to the expected theoretical result since  $2L \gg R^2 C_0$ .

## 2.4 Thin Film Resonator Analysis

Figures 2-5 and 2-6 illustrate the two basic thin film resonator (TFR) topologies used in this study. The difference between the two different topologies lie in the thin boron - doped  $p^+$  layer which lies directly below the

AlN piezoelectric layer as illustrated in Figure 2-6. This p<sup>+</sup> layer is used as an etch stop for a selective chemical etch. However, to obtain mass sensitivity for the TFR, the p<sup>+</sup> layer is also etched off resulting in two TFR topologies which are basically the same. It should be noted that the p<sup>+</sup> layer induces severe crystalline defects into the silicon lattice and thus impedes the fabrication of other active devices on the silicon substrate near the resonator.

The functionality of the aluminium nitride (AlN) piezoelectric TFR is similar to the conventional low frequency quartz crystal. However, the fundamental difference lies in the processing technology where the thin AlN film is formed by an additive deposition process rather than the mechanical extraction and trimming of the quartz crystal from a bulk crystal ingot. A complete analysis of the film growth and materials characterization is out of the scope of this study, however a number of theoretical and experimental studies have been reported [11,12,13,14]. Nevertheless, high quality AlN film deposition plays a crucial role in the operation of the TFR. The geometry of the TFR is basically composed of the AlN thin piezoelectric layer with its c-axis normal to the aluminium electrode contacts formed on the top and backside as illustrated in Figures 2-5 and 2-6. For a 1 GHz resonator, that is a series resonance of 1 GHz, the thickness of the AlN film is grown to be approximately 5 μm. The connection between the topside ground connection and the backside ground plane is accomplished by a capacitive coupling effect through the bulk of the silicon substrate. This coupling effect degrades the performance of the TFR since there is now a distributed resistance and larger parallel capacitance in the actual circuit model of the resonator. The resulting consequence of this parasitic coupling is higher loss and lower Q. A further parasitic complication of

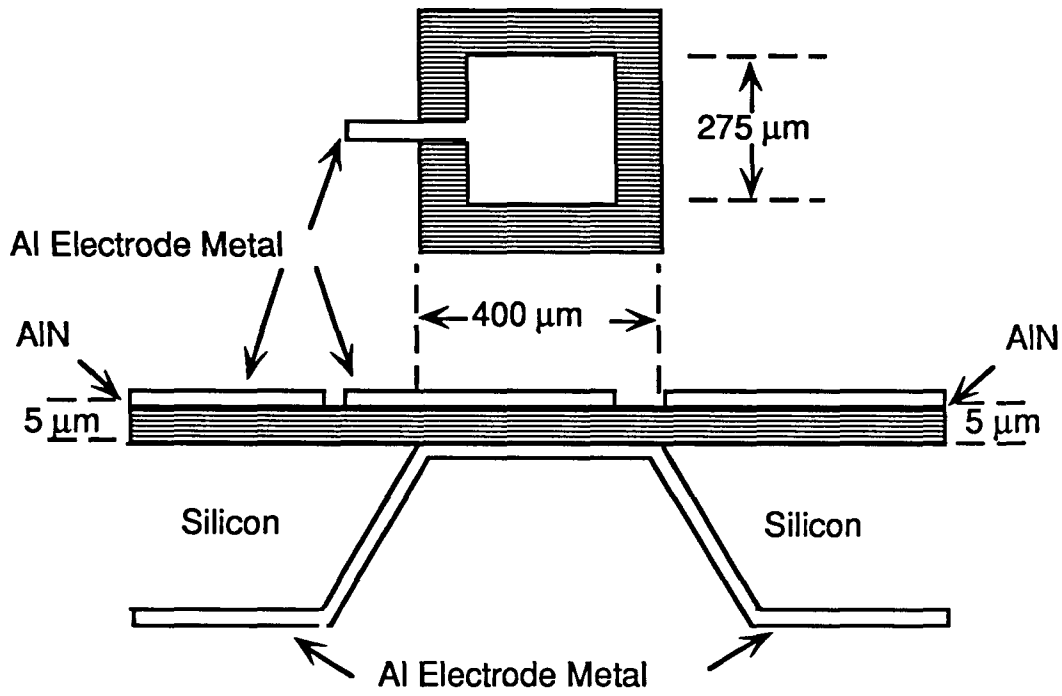


Figure 2-5. AIN thin film resonator topology

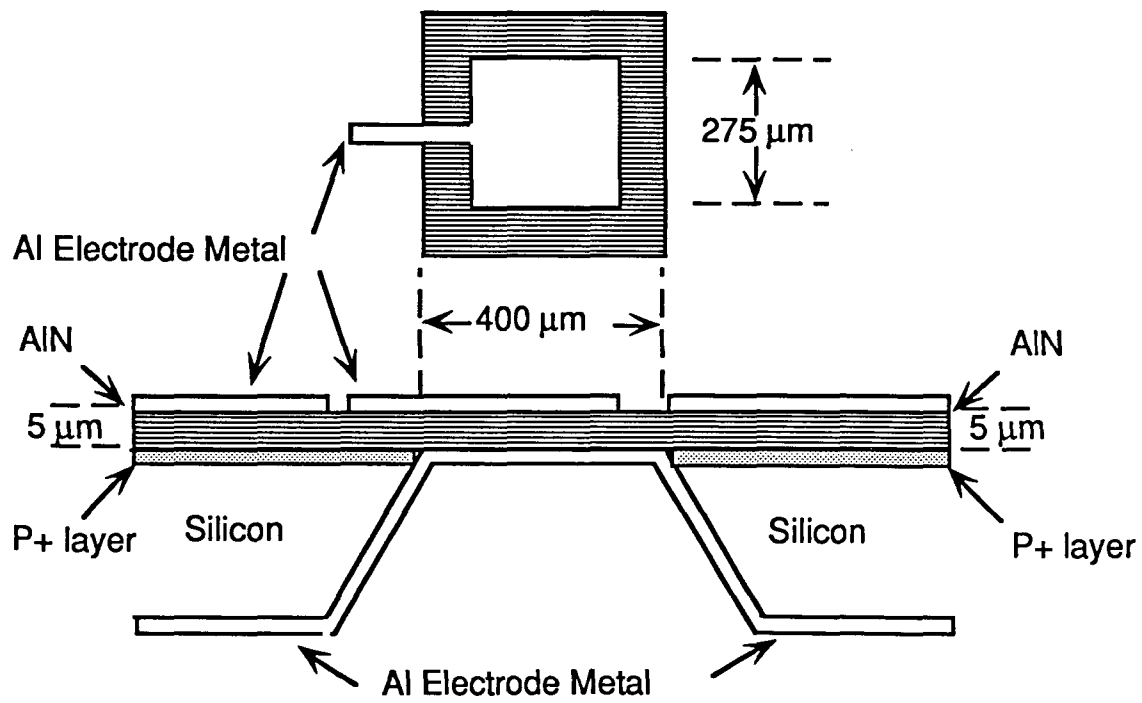


Figure 2-6. P+ Membrane AIN TFR Topology

this geometry is attributed to the piezoelectric film being uniformly deposited over the bulk silicon substrate. Spurious modes near the fundamental are generated and coupled into the overall resonator response since the probe contact pads also form a resonator between the topside probe pads and the capacitively coupled backside ground plane. This parasitic resonator can be hypothesized to be an overmoded structure with varying thickness due to the slope of the backside silicon etch and thus introduces various stray modes into the final resonator structure. Figure 2-7 illustrates the various proposed parasitics associated with this geometry.

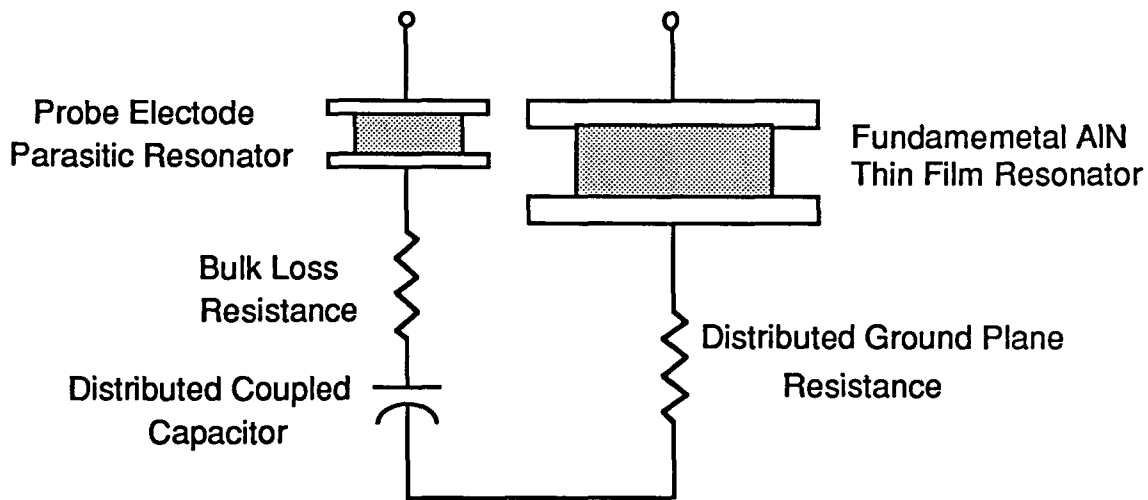


Figure 2-7. Parasitic Multiple Mode TFR Model

## 2.5. Resonator Measurement and Modeling

The resonator test system which was employed to extract S parameters from the resonators consisted of Cascade Microtech r.f. probes and the HP8510 network analyzer. The r.f. probes were used to make contact in the 50Ω system

with the probe pad electrodes on the resonator under test. Once the fundamental resonant frequency was found for the particular resonator, the frequency sweep on the HP8510 network analyzer was set for a narrow bandwidth window which contained both the resonant and anti-resonant frequencies. A one-port calibration on the  $50\Omega$  system was then performed which set the measurement phase plane to the edge of the r.f. coplanar probe contacts and accounted for any losses in the coaxial lines and connections up to the probe plane. This allows extremely accurate measurements for the resonators since all phase and magnitude measurements will be made with reference to the r.f. probe resonator pad. Swept frequency measurements were then made with the HP8510 network analyzer to obtain the S parameters which were then down loaded to a HP workstation via the GPIB interface bus. Once in the workstation, a data acquisition program stored the S parameters and performed calculations such as Smith chart plots, impedance magnitude and phase plots, resonant and anti-resonant frequency points, the phase slope near the resonant frequency, and Q calculations. The input impedance of the resonator at a particular frequency can be calculated from the measured one-port S parameters from equation (2.44).

$$Z_{in} = Z_o \frac{(1 + S_{11})}{(1 - S_{11})} = R + jX \quad (2.44)$$

The impedance magnitude and phase can then be found and the variation of Q as a function of frequency near resonance can be calculated from the impedance phase and equation (2.38) which simplifies down to equation (2.45) near series resonance:

$$Q = \frac{\omega}{2} \frac{\partial \theta}{\partial \omega} \Big|_{f_r} \quad (2.45)$$

The partial derivative of the impedance phase with respect to the frequency was found by means of a 5 point central difference approximation. The resulting calculation is quite noisy and thus a more accurate value of Q near series resonance can be found by doing a least squares fit near the resonant point at which the impedance phase is obtained.

The S parameter data can also be loaded into Libra™ which provides accurate solutions in the linear analysis, simulation and optimization of microwave and RF circuits. In this case, Libra™ will be employed to study the effects of various parasitics on the electrical behavior of the resonator and in addition, the optimizing routine will be used to extract the equivalent circuit modelling parameters. Appendix D contains a representative program listing used to find the equivalent circuit model for two single moded resonators.

Initially, the circuit to be simulated consisted of the Butterworth - Van Dyke equivalent circuit of Figure 2-3. The pre-optimized circuit values that were initially entered into the Libra™ circuit program were found by means of the basic relationships of Q, series resonance and parallel resonance in terms of the circuit model parameters as previously derived in section 2.3. The need for initial values arises from the fact that there probably exists several possible circuit solutions for the optimization, some of which are physically unrealizable (i.e. negative resistance and inductance values). However, the resulting simulation results on the Butterworth - Van Dyke equivalent circuit model were unsatisfactory and the inclusion of parasitics needed to be investigated. The

resulting circuit which closest simulates the measured electrical behavior of the AIN thin film resonator is illustrated on Figure 2-8.

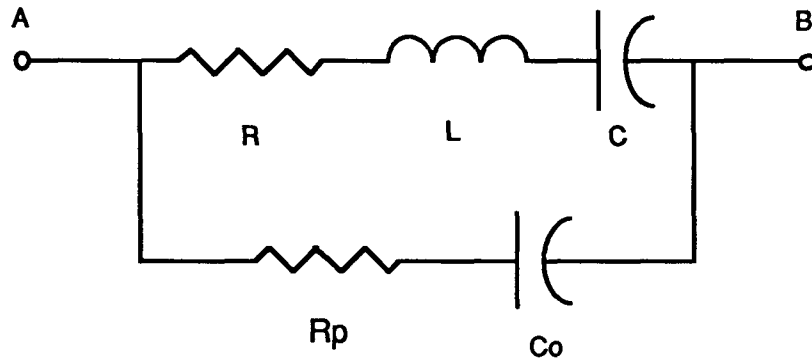


Figure 2-8. Equivalent circuit model of the AIN TFR with the inclusion of  $R_p$

The parasitic resistance,  $R_p$ , was needed in the modelling to account for the impedance magnitude behavior of the TFR near the parallel and anti-resonant frequencies. Without  $R_p$ , the impedance magnitude was extremely large at the anti-resonant frequency as theoretically expected but experimentally unfounded. The parasitic resistance can physically be thought of as bulk losses in the AIN and silicon characteristic of the capacitive coupling effect between the ground plane and electrode contacts and thus not related to the motional parameters of the piezoelectric thin film. In order to verify this model, two thin film resonators were modeled which had topologies of Figure 2-5. It should be noted that the parasitic resistance did not alter the resonant frequencies significantly and thus the equations derived in section 2-3 are still applicable. Figures 2-9a, 2-9b, and 2-9c are the Smith chart, impedance magnitude plot, and impedance phase plot, respectively, of the first optimized resonator which will be referred to as K12 after its position on wafer Bray18-63c. The smooth

curve in each plot is the model response while the jagged curve represents the actual measured data. Figures 2-10a, 2-10b, and 2-10c are the corresponding Smith chart and impedance magnitude and phase plots for resonator I12 also found on wafer Bray18-63c. Without the inclusion of  $R_p$ , the impedance magnitude would have been substantially larger near series and parallel resonance. The effect  $R_p$  has on the impedance magnitude near series and parallel resonance is to lower its value.  $R_p$  has little effect on the impedance phase plot. It is interesting to note that in both cases the value of  $R_p$  optimized out to be almost exactly 10 ohms. Table 2-1 contains the simulated values of the impedance parameters of Figure 2-8. Tables 2-2a and 2-2b are a listing of the various frequencies of interest and Q values which were calculated from the simulated impedance parameter values. Table 2-3 contains a listing of the impedance magnitudes which occur at the various resonant frequencies.



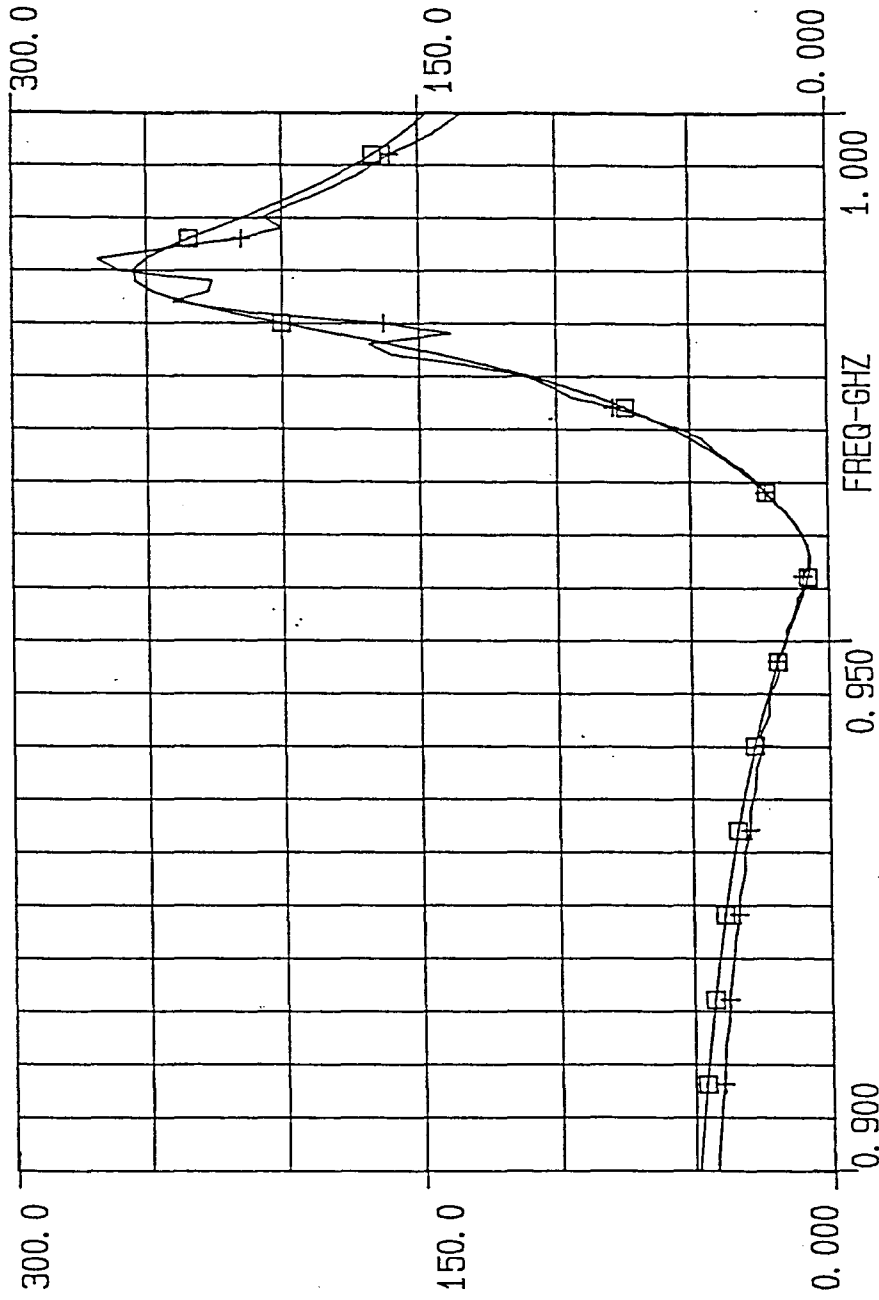


Figure 2-9b. Impedance magnitude plot for K12

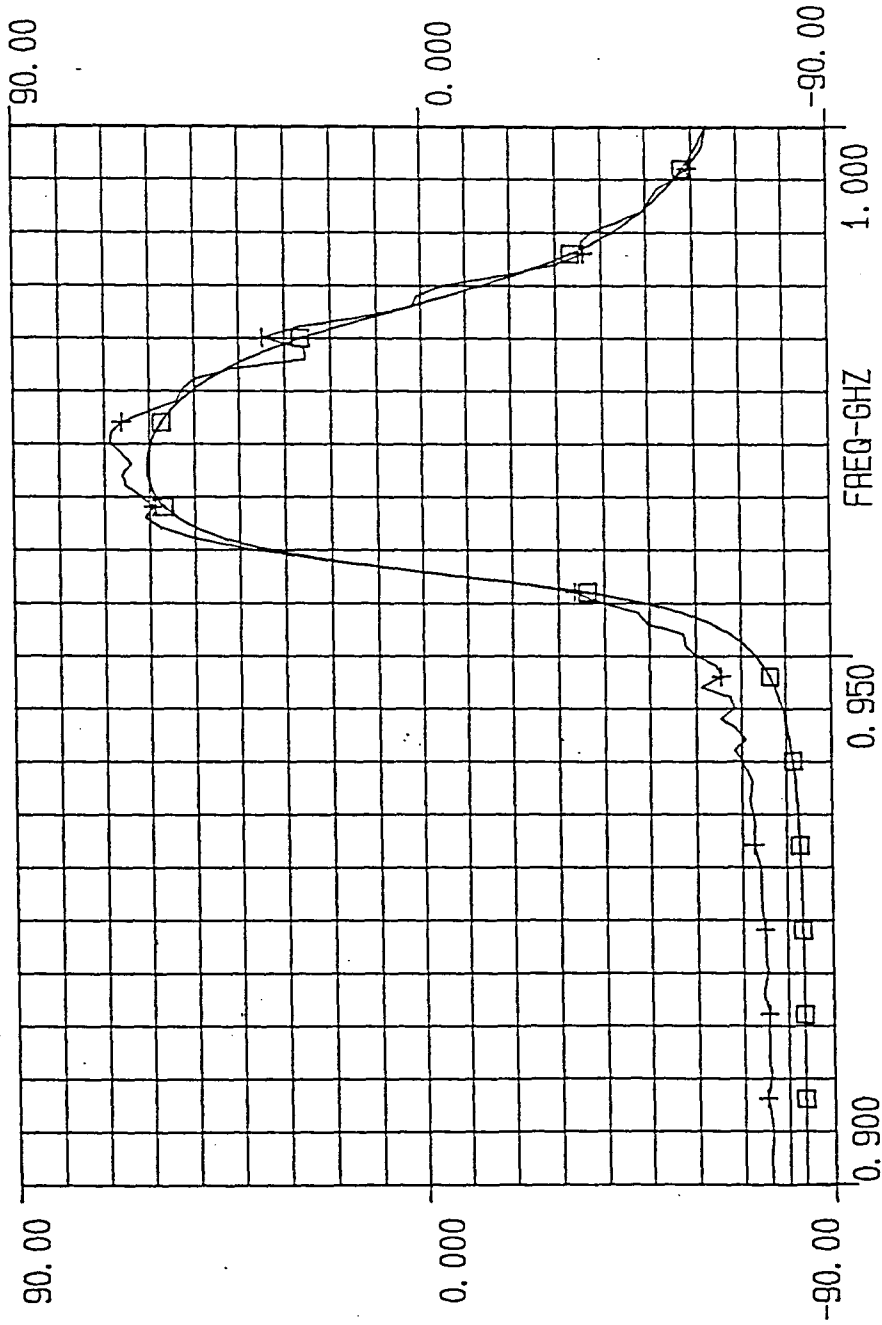


Figure 2-9c. Impedance phase plot for K12

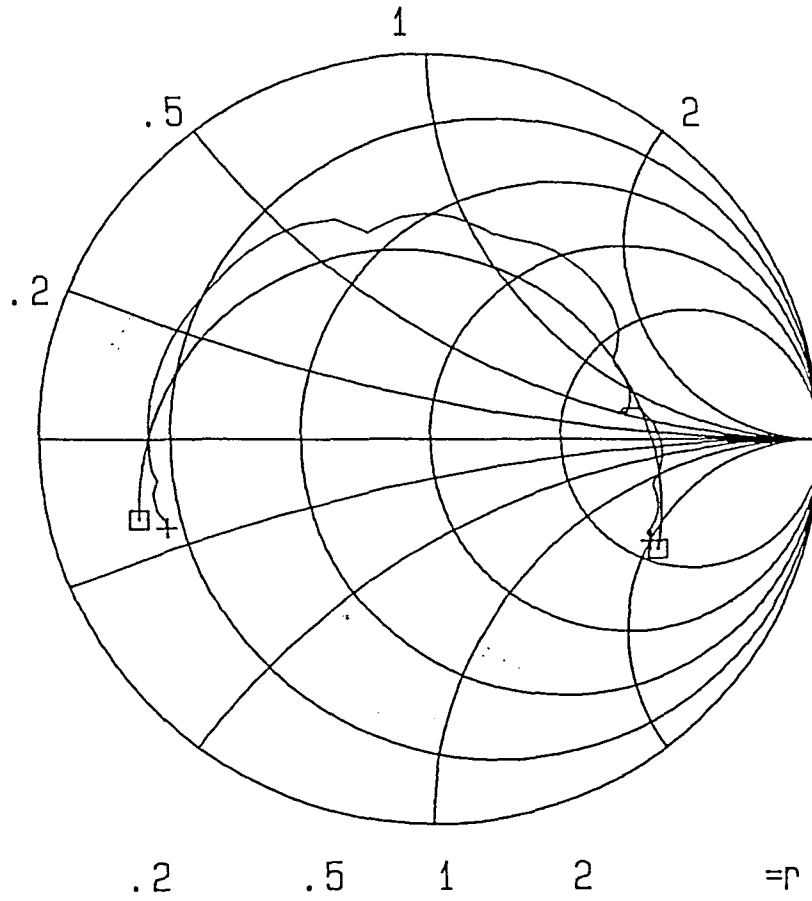


Figure 2-10a. Smith chart plot for I12

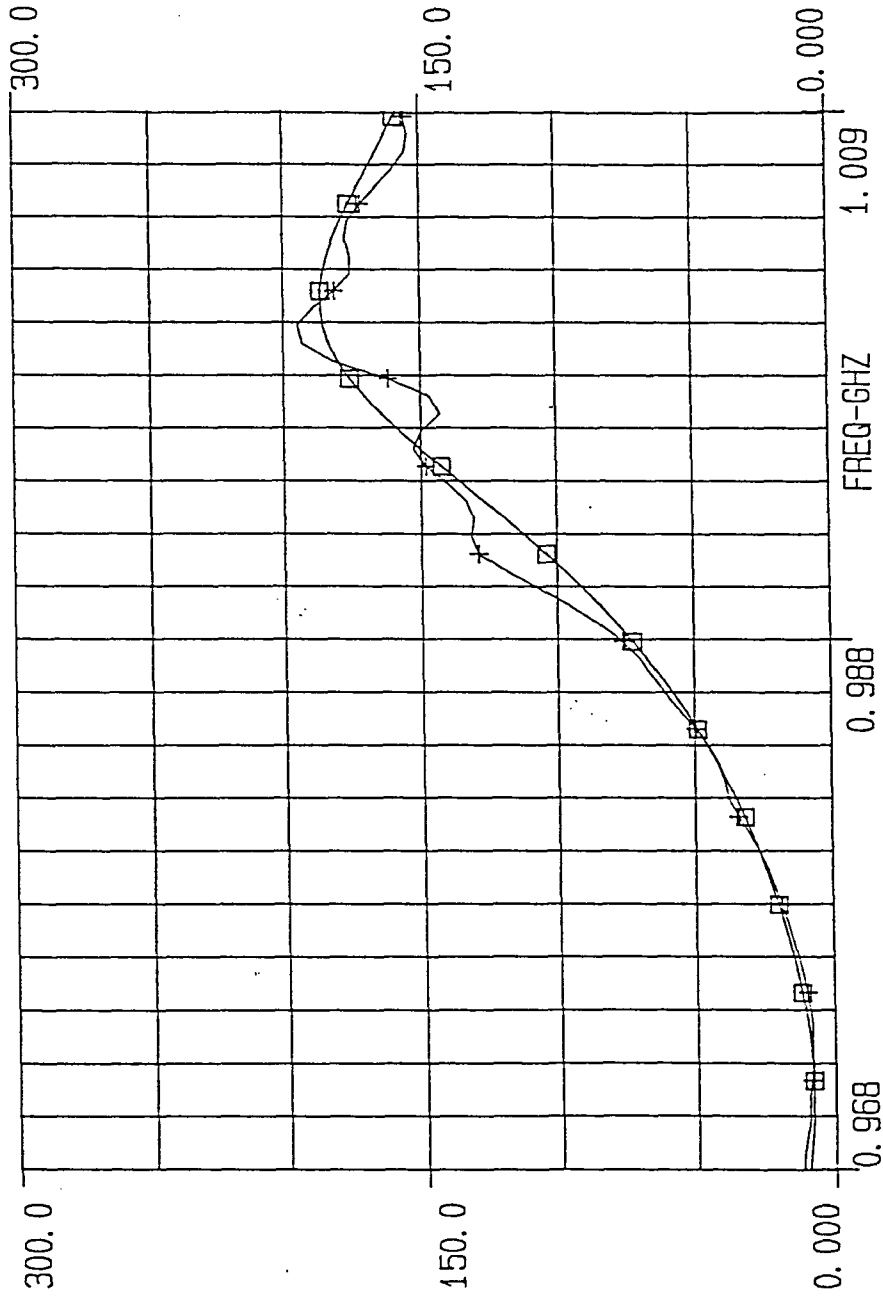


Figure 2-10b. Impedance magnitude plot for I12

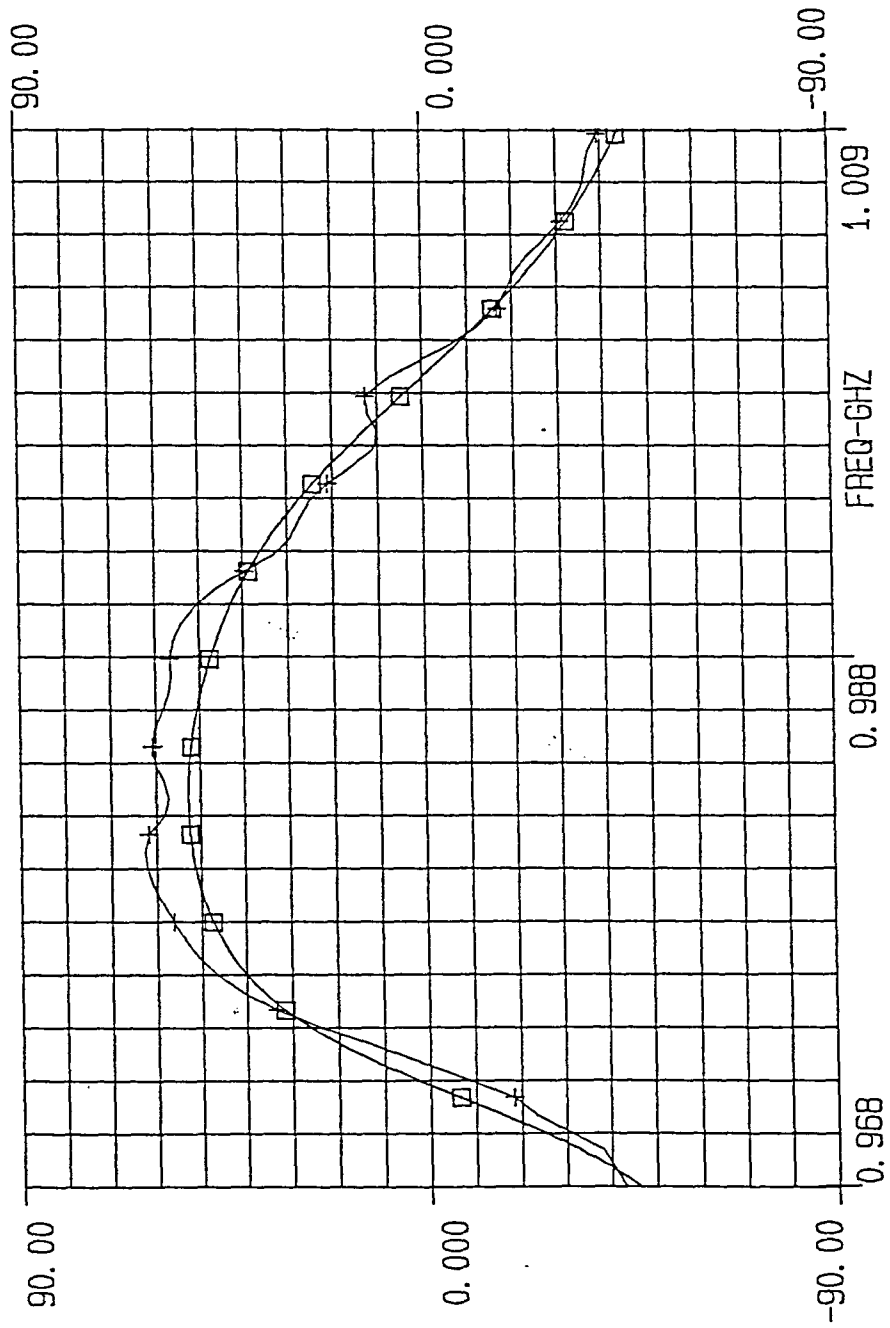


Figure 2-10c. Impedance phase plot for I12

Table 2-1. Touchstone simulation impedance parameter results

AIN Thin Film Resonator	R ( $\Omega$ )	L (nH)	C (pF)	Co (pF)	Rp ( $\Omega$ )
Bray 18-63c k12	6.899	203.901	0.1355	2.525	10.0
Bray 18-63c l12	8.049	163.317	0.1644	2.841	10.0

Table 2-2a. Calculated resonant frequency results

AIN Thin Film Resonator	$f_r$ (MHz)	$f_s$ (MHz)	$f_a$ (MHz)	$f_p$ (MHz)
Bray 18-63c k12	958.20144	957.91587	982.97098	983.26402
Bray 18-63c l12	971.89268	971.33380	998.46758	999.04207

Table 2-2b. Calculated impedance frequency points and Q results

AIN Thin Film Resonator	$f_{m,\theta}$ (MHz)	$f_{min,z}$ (MHz)	$f_{max,z}$ (MHz)	$Q_s$	$Q_p$
Bray 18-63c k12	970.58570	957.63369	983.88175	177.8	182.6
Bray 18-63c l12	985.18013	970.78682	999.98486	123.8	127.4

Table 2-3. Resonant frequency impedance calculations

AIN Thin Film Resonator	$Z_{\omega_r}$ ( $\Omega$ )	$Z_{\omega_s}$ ( $\Omega$ )	$Z_{\omega_a}$ ( $\Omega$ )	$Z_{\omega_p}$ ( $\Omega$ )
Bray 18-63c k12	6.976	6.824	589.514	596.139
Bray 18-63c l12	8.212	7.895	382.893	390.665

### 3. MASS DETECTION ANALYSIS

#### 3.1. Mass Loading Resonator Analysis

The concept of mass detection by the piezoelectric resonator is based upon the resonant frequency shift due to the application of mass upon the piezoelectric electrode. In most analysis, the electrode is considered as part of the intrinsic piezoelectric layer and thus the frequency shift is solely due to the added mass. Sauerbrey is credited with first proposing the resonant frequency shift of an oscillator controlled by a piezoelectric crystal due to the application of a thin layer of mass. The resonant frequency shift could then be used to measure the thickness and added mass for which he came up with the relation [9] :

$$\Delta f = - \left( \frac{2 f_p^2}{\rho_p v_p A} \right) \Delta m_f \quad (3.1)$$

where  $f_p$  is the fundamental resonant frequency before the application of the mass,  $\rho_p$  is the density of the piezoelectric crystal,  $A$  is the active area,  $v_p$  is the acoustic phase velocity of the mode of resonance in the piezoelectric film, and  $\Delta m_f$  is the added mass of the thin film. The fundamental resonant frequency of a piezoelectric crystal vibrating in thickness longitudinal mode is given by:

$$f_p = \frac{V_p}{2 l_p} \quad (3.2)$$

where  $l_p$  is the thickness of the piezoelectric layer. The Sauerbrey relation makes clear that only the addition of the mass on the electrode affects the resonant frequency and that for a crystal of uniform thickness only the mass per unit area is relevant. All other properties of the deposited film appear to not contribute to the resonant frequency shift.

However, the true physical behavior of the piezoelectric-film composite resonator can best be understood in terms of the acoustic wave properties of the compound device. Miller and Bolef [15] were the first to apply a continuous-wave acoustic analysis to a one-dimensional two-material composite resonator. The theory behind their analysis was that since the resonant frequency of an unloaded piezoelectric resonator is related to its elastic constant, the elastic properties of the deposited film should be related to the frequency shift. This idea strayed from the traditional belief that the acoustic wave of the resonator did not propagate into the film and thus no energy was stored in the layer during oscillation. The condition for oscillation of the composite resonator in the absence of acoustical attenuation which was formulated by Miller and Bolef can be expressed in simplified form [16] by:

$$\tan\left(\frac{\pi f_c}{f_p}\right) = -\frac{\rho_f v_f}{\rho_p v_p} \tan\left(\frac{\pi f_c}{f_f}\right) \quad (3.3)$$

where the  $f$ ,  $c$ , and  $p$  subscripts are related to the film, composite, and piezoelectric material properties, respectively. The  $v$  term is the acoustic phase velocity in the designated region,  $\rho$  the density, and  $f$  is the fundamental resonant frequency in each layer as described by equation (3.2). Equation (3.3) contains the factor  $\rho_f v_f / \rho_p v_p$  which is the ratio between the acoustic

impedances of the deposited film and the piezoelectric layer and thus materials with different acoustic impedances will obey different mass thickness-frequency relationships.

Applying the small mass approximation [16] for which  $f_c \ll f_f$  and  $(f_p - f_c) \ll f_p$  to equation (3.3) and utilizing the trigonometric identity:

$$\tan\left(\frac{\pi f_c}{f_p}\right) = -\tan\left(\frac{\pi(f_p - f_c)}{f_p}\right) \quad (3.4)$$

the tangent functions of equation (3.3) can be Taylor expanded in a Maclaurin series since the arguments are very small and keeping the first term simplifies down to:

$$\frac{f_c}{f_p} = \left(1 + \frac{\rho_f v_f f_p}{\rho_p v_p f_f}\right)^{-1} \quad (3.5)$$

The acoustic phase velocity for the longitudinal mode in the film and piezoid layers given by equation (3.2) can be substituted into equation (3.5) to yield:

$$\frac{f_c}{f_p} = \left(1 + \frac{\rho_f l_f}{\rho_p l_p}\right)^{-1} \quad (3.6)$$

For most practical applied films, the density between the piezoelectric and applied film is not going to vary more than one order of magnitude. A further thin film approximation can be applied to equation (3.6) if  $\rho_f l_f / \rho_p l_p \ll 1$  and the binomial expansion  $(1 + x)^{-1} \approx 1 - x$  for  $x \ll 1$  is utilized which results in:

$$\frac{f_c}{f_p} = 1 - \frac{\rho_f l_f}{\rho_p l_p} \quad (3.7)$$

The term  $\rho_f l_f$  is the added mass per unit area and thus equation (3.7) can be easily simplified down to the Sauerbrey relation given by equation (3.1). The linear frequency shift-mass relationship under the small mass and thin film approximation given by equation (3.7) has been investigated and found to be accurate to frequency shifts of 2% of the fundamental frequency [16]. Thus, a 1 GHz thin film resonator is allowed 20 MHz of resonant frequency shift under this approximation.

Equation (3.7) can be written in a more useful form given by:

$$\frac{\Delta f}{f_o} = - \frac{\rho_f l_f}{\rho_p l_p} = - \frac{\Delta m}{m_o} \quad (3.8)$$

where the subscript  $p$  is replaced by  $o$  for generality. Equation (3.8) is the useful linear relation used to determine the uniformly distributed added mass per unit area,  $\Delta m$ , on the resonator electrode by virtue of the resonant frequency shift  $\Delta f$ . The term  $m_o$  is the mass per unit active area of the piezoelectric crystal ( $\rho_p l_p$ ).

The mass sensitivity,  $S_m$ , for the bulk-acoustic-wave resonator is defined as [17]:

$$S_m = \lim_{\Delta m \rightarrow 0} \frac{\Delta f}{f_o} \frac{1}{\Delta m} \quad (3.9)$$

where  $\Delta m$  is the mass per unit area. Comparing equation (3.9) to (3.8), the mass sensitivity for the fundamental resonant mode is found to be:

$$S_m = \frac{-2}{\rho \lambda} \quad (3.10)$$

where the wavelength  $\lambda$  is twice the piezoelectric crystal thickness. The units for the sensitivity are typically  $\text{cm}^2/\text{g}$  and thus a high sensitivity is desirable for low mass detection. For a highly sensitive bulk-acoustic-wave resonator, the resonant frequency should be made as high as possible by using a thin piezoelectric layer.

The utilization of the bulk-acoustic-wave resonator as a highly sensitive chemical sensing device is based upon the mass sensing theory previously described. Initially, the application of the thin absorbant coating on the TFR electrode surface produces a negative frequency shift due to the acoustic cavity of the added thin film. If the thickness and density of the applied thin film is known, the experimental mass sensitivity can be calculated from equation (3.9). The theoretical mass sensitivity of the TFR can be calculated from equation (3.10) for comparison. Upon exposure of the absorbant coated TFR to a gas phase analyte, the resonant frequency continues to shift downward from which the absorbed mass can be found from by a slight modification to equation (3.8) [18]:

$$\frac{\Delta f}{\Delta f_0} = - \frac{\Delta m}{\Delta m_0} \quad (3.11)$$

where  $\Delta f$  and  $\Delta m_0$  are the resonant frequency shift and added mass of the thin absorbant coating and  $\Delta f$  and  $\Delta m$  are the resonant frequency shift and absorbed mass of the gas phase analyte. However, this approximation is not a true representation of the added mass of the gas phase analyte on the absorbant coating. The gas phase analyte does not increase the length of the effective acoustic cavity of the resonator by a significant amount such that it would cause a resonant frequency shift. Instead, the resonant frequency shift is attributed to the change in density of the thin absorbant coating as shown in equation (3.8). The thin film absorbs the gas phase analyte and becomes more dense without changing its physical thickness resulting in a negative resonant frequency shift.

The important point to be stressed when considering the above analysis is the low-mass, loss-less thin film approximation. When the overlayer becomes lossy, the analysis becomes much more complex. Crane and Fischer [19] calculated a frequency-loading response for composite resonant system by treating the lossy overlayer as a lossy transmission line coupled to a lossless transmission line representing the quartz. However, the AIN TFR is a fairly low Q device in comparison to the quartz crystal resonator and thus Crane and Fischer's analysis must be altered to include loss in the piezoelectric film as done in the general analysis by Kanzazawa [20]. The shortcoming in all these analysis is the omission of the non-isotropic effects of the effective elastic and dielectric constants of the piezoelectric film. When these are considered, the complete one-dimensional analysis consists of transfer matrix equations of the arbitrary orientated layered piezoelectric structure resulting in an exact solution of the electrical admittance appearing between the electrodes for any frequency as well as the determination of the entire resonance frequency spectrum. This

type of analysis is out of the scope of this study, however the theory of the multi-layer transfer matrix solution has been thoroughly investigated by Notwostry and Benes [21], Shick and Tiersten [22], and Adler [23], [24], [25].

### 3.2. Parasitic Frequency Effects

The principle utility of the AlN TFR lies in its ability to be fabricated on the same silicon substrate as the surrounding active micro-electronic devices such as transistors thus allowing oscillator and signal processing electronic fabrication on the same microchip. The concept of integrated oscillator design using the TFR has been previously investigated and realized in monolithic form [3]. Thus, the potential for a complete miniaturized chemical sensing system exists by utilizing the present TFR technology and applying it so as to detect an oscillator frequency shift by virtue of the mass loading - resonant frequency shift effect. However, in the development stages of the chemical sensor, the TFR will be tested in component form resulting in additional parasitics due to wire bonds and the mounting package. The resulting one-port circuit structure which accounts for the stray parasitic effects is illustrated in Figure 3.1.

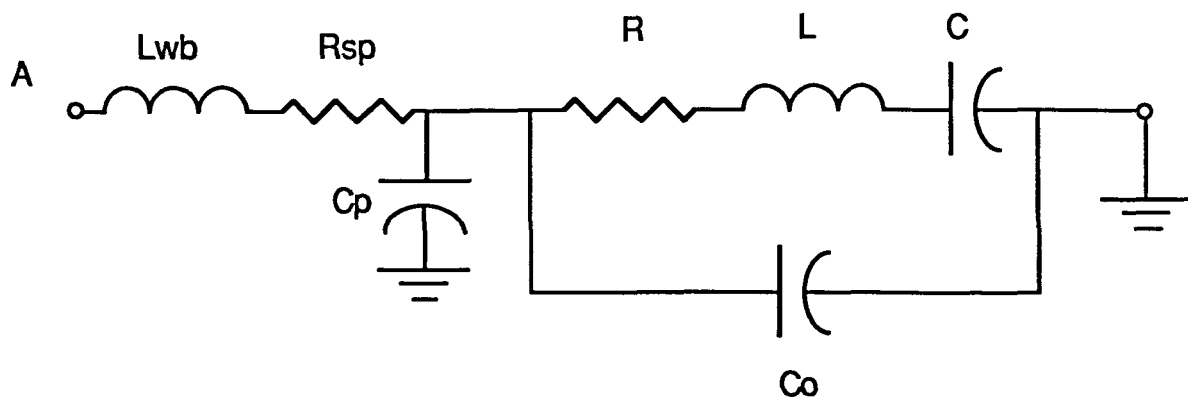


Figure 3.1. Parasitic Packaging Model

Figure 3.1 considers the packaging capacitance,  $C_p$ , the wirebond inductance  $L_{wb}$  and series parasitic resistance  $R_{sp}$ . When the TFR is analyzed as a one-port, the packaging capacitance is seen to be in parallel with the static bulk capacitance,  $C_0$ , of the TFR resulting in a total parallel capacitance  $C_T$  which is the sum of  $C_0$  and  $C_p$ . Since both the resonant and anti-resonant frequencies of the TFR depend on  $C_T$  to a certain extent as given in equations (2.19) and (2.20), the variation of  $C_p$  and the capacitive coupling effect which is reflected in the value of  $C_0$  must influence the resonant behavior of the TFR. In some oscillator applications, the value of  $C_T$  is deliberately changed which allows the oscillator frequency to be tuned in a limited bandwidth.

The dependence of the resonant and anti-resonant frequencies on the value of  $C_T$  can be found by differentiating equations (2.22) and (2.23) with respect to  $C_T$  resulting in the sensitivity equations (3.12) and (3.13). The frequency sensitivity of the anti-resonant frequency due to  $C_T$  is expected to be much higher than that of the resonant frequency due to the parallel resonant effect of  $C_T$  with the series motional impedances. The dependence of the resonant and anti-resonant frequencies on  $C_T$  from equations (3.12) and

$$\frac{df_r}{dC_T} = \frac{\sqrt{2}}{8\pi} \frac{-\left(\frac{1}{C_T^2 L}\right) - \frac{\frac{4}{C C_T^2 L^2} + \frac{2\left(\frac{-2}{C} - \frac{1}{C_T} + \frac{R^2}{L}\right)}{C_T^2 L^2}}{2\sqrt{\frac{\left(\frac{-2}{C} - \frac{1}{C_T} + \frac{R^2}{L}\right)^2}{L^2} - \frac{4\left(\frac{1}{C} + \frac{1}{C_T}\right)}{C L^2}}}}{\sqrt{\frac{2}{C L} + \frac{1}{C_T L} - \frac{R^2}{L^2}} - \sqrt{\frac{\left(\frac{-2}{C} - \frac{1}{C_T} + \frac{R^2}{L}\right)^2}{L^2} - \frac{4\left(\frac{1}{C} + \frac{1}{C_T}\right)}{C L^2}}} \quad (3.12)$$

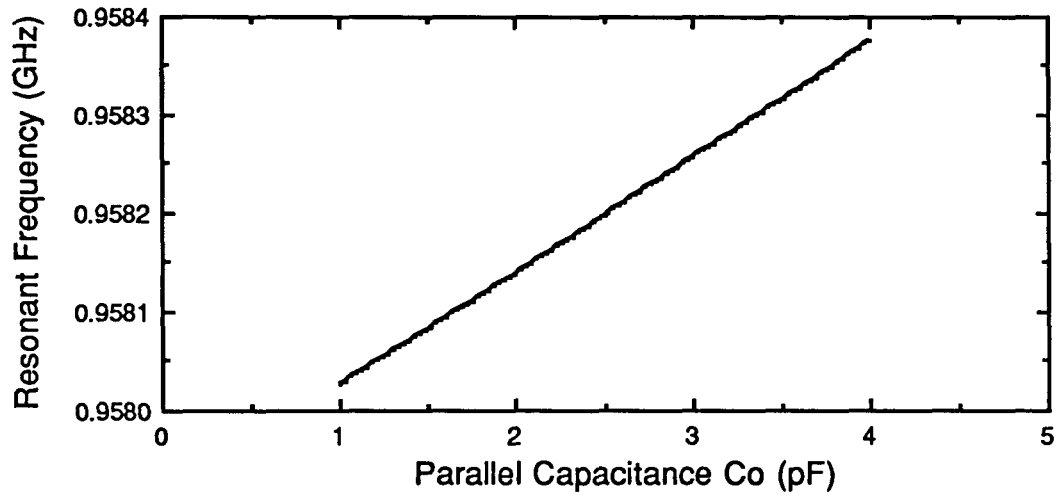
$$\frac{df_a}{dC_T} = \frac{\sqrt{2}}{8\pi} \frac{-\left(\frac{1}{C_T^2 L}\right) + \frac{\frac{4}{C C_T^2 L^2} + \frac{2\left(-\frac{2}{C} - \frac{1}{C_T} + \frac{R^2}{L}\right)}{C_T^2 L^2}}{2\sqrt{\frac{\left(-\frac{2}{C} - \frac{1}{C_T} + \frac{R^2}{L}\right)^2}{L^2} - \frac{4\left(\frac{1}{C} + \frac{1}{C_T}\right)}{C L^2}}}}{\sqrt{\frac{2}{C L} + \frac{1}{C_T L} - \frac{R^2}{L^2}} + \sqrt{\frac{\left(-\frac{2}{C} - \frac{1}{C_T} + \frac{R^2}{L}\right)^2}{L^2} - \frac{4\left(\frac{1}{C} + \frac{1}{C_T}\right)}{C L^2}}} \quad (3.13)$$

(3.13) is not easily verified; however if the parallel resonant frequency is analyzed which is closely related to  $f_a$ , an approximate inverse square relation exists as seen in equation (3.14).

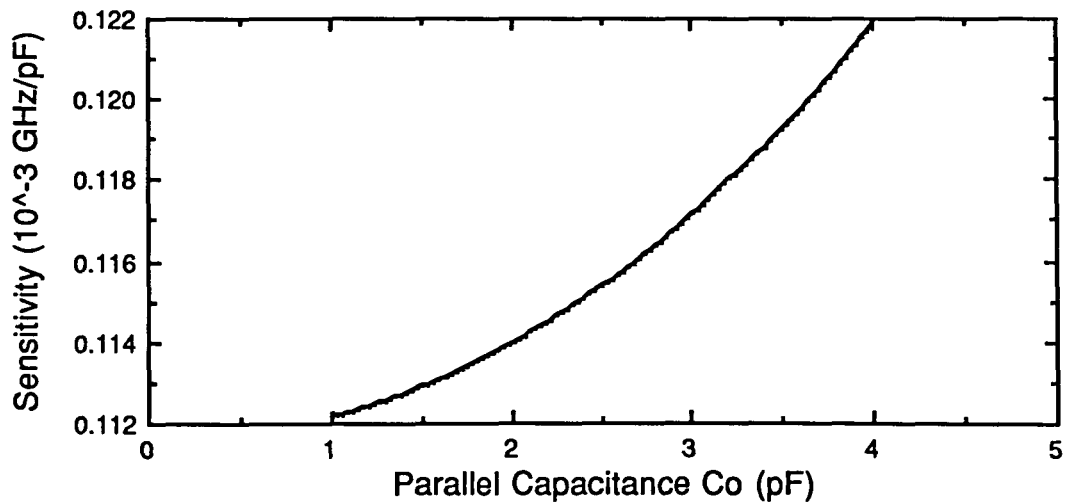
$$\frac{df_p}{dC_T} \approx \frac{1}{2} \frac{C f_p}{C_T^2} \quad (3.14)$$

The resonant and anti-resonant frequency dependence and sensitivities with respect to  $C_T$  can be graphically analyzed from Figures 3-2 and 3-3. These figures are the graphical analysis of the resonant frequency equations (2.22) and (2.23) and the sensitivity equations (3.12) and (3.13). The motional impedance values which were used in these equations were the typical values found in table 1 for Bray 18-63c k12 with the omission of  $R_p$ . Figures 3-2 and 3-3 illustrate a two order of magnitude difference between the anti-resonant and resonant frequency sensitivity as expected.

The utility of a shunt tuning capacitance that results in the desired frequency shifts of the resonator must be carefully considered since there is a maximum value of  $C_T$  for which the circuit can be used if a required inductive



(a)



(b)

Figure 3-2. Resonant frequency dependence on  $C_o$ : (a) resonant frequency vs  $C_o$ ; (b) resonant frequency  $C_o$  sensitivity

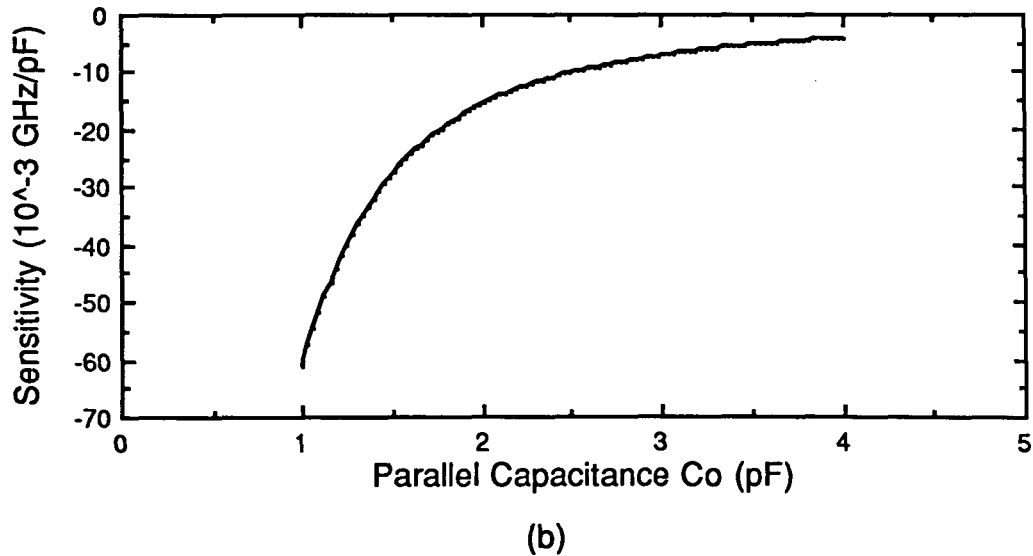
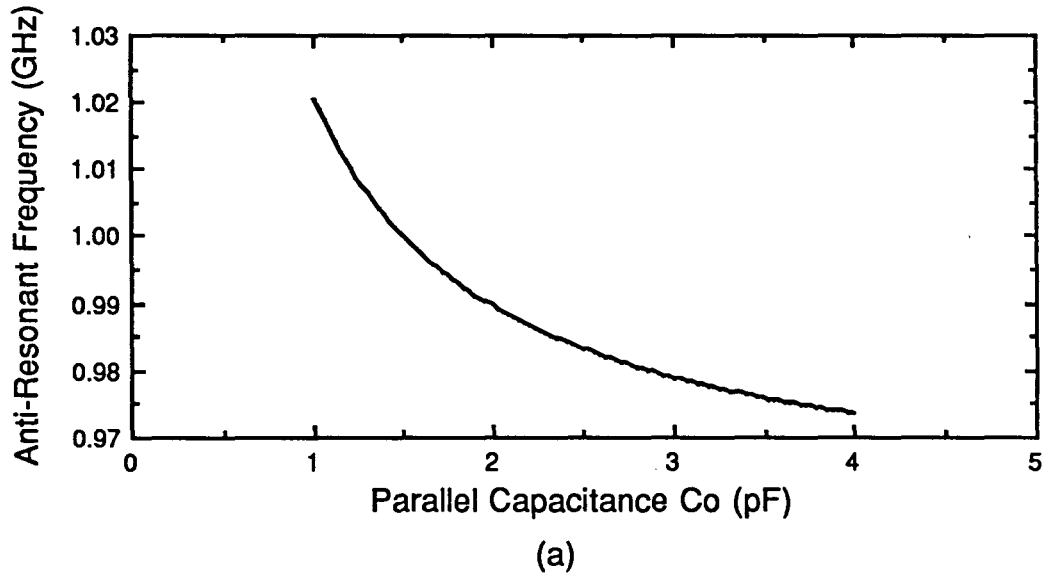


Figure 3-3. Anti-resonant frequency dependence on  $C_o$ : (a) anti-resonant frequency vs  $C_o$ ; (b) anti-resonant frequency  $C_o$  sensitivity

reactance is needed. As the value of  $C_T$  is increased, the resonant and anti-resonant frequencies move closer to each other until a point is reached for which only one zero-phase frequency exists. This condition is best understood by evaluating the condition for resonance as given earlier in equation (2.20) which is repeated in equation (3.15):

$$\omega^4 C^2 L^2 C_T - 2\omega^2 C C_T L - \omega^2 C^2 L + \omega^2 R^2 C^2 C_T + C + C_T = 0 \quad (3.15)$$

The condition for the existence of real roots for this equation using the quadratic equation is that the discriminant ( $b^2 - 4ac$ ) be greater than or equal to zero [7].

This condition results in:

$$(4R^2C^3L - R^4C^4) C_T^2 + 2 R^2C^4 C_T L - C^4 L^2 \leq 0 \quad (3.16)$$

Solving equation (3.16) for real  $C_T$ :

$$C_T \leq \frac{LCR - 2L\sqrt{LC}}{R^3C - 4LR} \quad (3.17)$$

However, for most practical resonators  $2L(LC)^{1/2} \gg LCR$  and  $4LR \gg R^3C$ , thus equation (3.17) can be reduced to:

$$C_T \leq \frac{2L\sqrt{LC}}{4LR} = \frac{1}{2\omega_s R} = \frac{Q_s C}{2} \quad (3.19)$$

Equation (3.19) sets the limit for maximum parallel capacitance  $C_T$  in terms of the quality factor of the resonator if a zero-phase resonance is to occur.

The determination of  $C_T$  or  $C_0$ , depending on the situation, can usually be measured fairly accurately by measuring the impedance of the resonator at a frequency which corresponds to 10% below and above the expected resonant frequencies and averaging these values. However, to de-embed this capacitance and find the motional impedances is not so simple. The standard data reduction method [10] consists of initially finding the admittance of the resonator. The admittance for the TFR of Figure 3-1 omitting any series parasitics can be written as follows:

$$Y = G + jB = \frac{R}{R^2 + (\omega L - 1/\omega C)^2} + j \frac{-(\omega L - 1/\omega C)}{R^2 + (\omega L - 1/\omega C)^2} + j\omega C_T \quad (3.20)$$

The admittance can be transformed and rewritten giving [26]:

$$\left(G - \frac{1}{2R}\right)^2 + (B - \omega C_T)^2 = \frac{1}{4R^2} \quad (3.21)$$

This is an equation of a circle in the admittance plane of radius  $1/2R$  centered at  $G = 1/2R$  and  $B = \omega C_T$ . The data manipulation process consists of finding the resonance of the resonator, take measurements around the resonance, fitting a circle to the admittance data and then fitting a linear function to the rate of change of frequency around the circle. The effect of  $C_T$  is simply to move the circle along the B axis and thus can be mathematically removed by moving the circle such that the center lies on the G axis. Once this is done, all that is left is

the motional parameters which can be calculated by the variation of frequency around the circle. The curve-fitting routine consists of a two step process in which the initial values are calculated by an analytical multiple linear regression. These initial values are then used in an iterative technique which minimizes the sum of the squares of the differences of the radii.

Once the admittance points are fitted to a circle and the effects of  $C_T$  are eliminated, the motional parameters can be deduced by fitting a linear curve to admittance phase [26]:

$$\begin{aligned}\tan \theta = B(\omega)/G(\omega) &= \frac{-\left(\omega L - \frac{1}{\omega C}\right)}{R} \\ &\approx a (f_{ref} - f) + b\end{aligned}\quad (3.22)$$

where

$$a = 2Q/f_s \quad (3.23)$$

and

$$b = \frac{2Q (f_s - f_{ref})}{f_s} \quad (3.24)$$

The value of  $f_{ref}$  is a frequency chosen slightly above  $f_s$ . Thus, the complete equivalent circuit can be found by the following relationships:

$$f_s = \frac{b}{a} + f_{ref} \quad (3.25)$$

$$Q = \frac{f_s a}{2} \quad (3.26)$$

$$R = \frac{1}{2 r} \quad (3.27)$$

$$C_T = \frac{y_0}{2 \pi f_s} \quad (3.28)$$

$$C = \frac{1}{2 \pi f_s R Q} \quad (3.29)$$

$$L = \frac{1}{C (2 \pi f_s)^2} \quad (3.30)$$

where the radius of the circle is  $r$  and is centered at  $(x_0, y_0)$ . A complete and detailed analysis of this approach can be found in references [26] and [27].

A second approach to finding the motional parameters which is widely used in industry involves converting the resonator admittance to impedance after the effects of the parallel capacitance  $C_T$  are mathematically removed [10], [28]. The circuit which is left is the series arm of the resonator where the real part is the motional resistance and the imaginary component, the reactance  $X$ , is the sum of the capacitance and inductance. The values of the reactance are then fitted to a polynomial function of frequency. For this circuit, the value of the series resonant frequency is where the reactance goes to zero leaving only the motional resistance. This allows the calculation of  $r$  and  $f_s$  from the polynomial function of frequency. The motional inductance can be calculated from the reactance expression:

$$L = \frac{1}{4\pi} \frac{dX}{df} \text{ evaluated at } f_s \quad (3.31)$$

The motional capacitance can then be calculated using the values of the series resonant frequency and motional inductance:

$$C = \frac{1}{(2\pi f_s)^2 L} \quad (3.32)$$

and the Q factor can be calculated from equation (3.29). In order for this approach to function properly, the frequency behavior of the resonator under test must be fairly smooth with no irregularities or spurs near series resonance due to the reactance derivative used to find the motional inductance as given in equation (3.31).

When the effects of a series parasitic resistance gets included in the analysis, the situation becomes much more complicated. A curve-fitting analysis for this problem was not attempted however, the effects of series resistance can be studied graphically. As the series parasitic resistance increases, the admittance circle gets smaller and moves away from the susceptance ordinate. Figure 3-4 is an example of this effect where the admittance of a TFR model for Bray 18-63c K12 was plotted for series parasitic resistances of 0 and 10 ohms. The impedance circle with the larger radius represents the 0 ohm series resistance while the smaller impedance circle has a series parasitic resistance of 10 ohms. The shifting effect of the circle away from the susceptance ordinate is not so clearly noticed however it does exist.

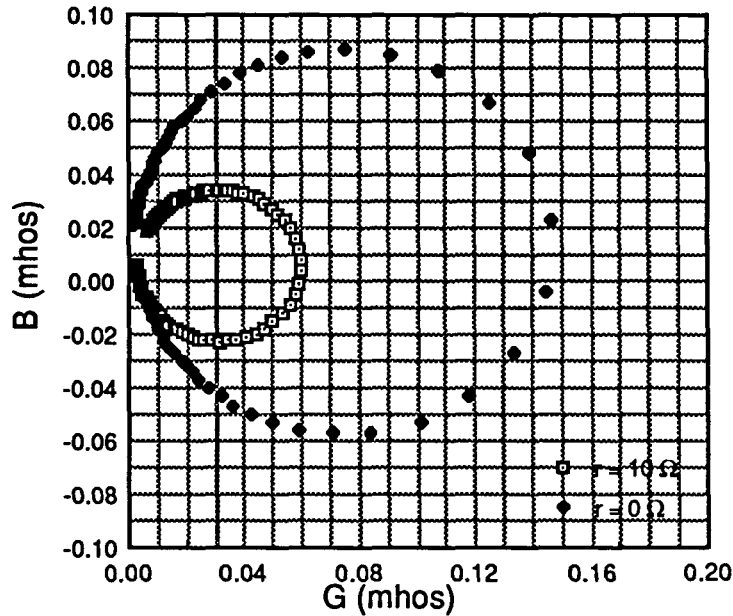


Figure 3-4. Admittance circle variation as a function of series parasitic resistance for  $r = 0$  and  $10 \Omega$

Figure 3-5 illustrates an actual locus of admittance points for data taken on a photo-resist coated TFR at methanol exposure times of 0 and 24 minutes. The admittance circle for the 24 minute MeOH exposure is shifted clockwise as compared to the initial admittance circle. This is characteristic of the resonant frequency shift due to mass loading of the TFR. Also, the 24 minute admittance circle has been shifted and its radius decreased which is probably due to the series motional resistance  $R$  increasing. The increase in the series motional resistance can be associated with a decreasing  $Q$  which was noticed in this case, however no conclusions can be drawn at this point since the variation of the motional inductance and motional capacitance is not known.

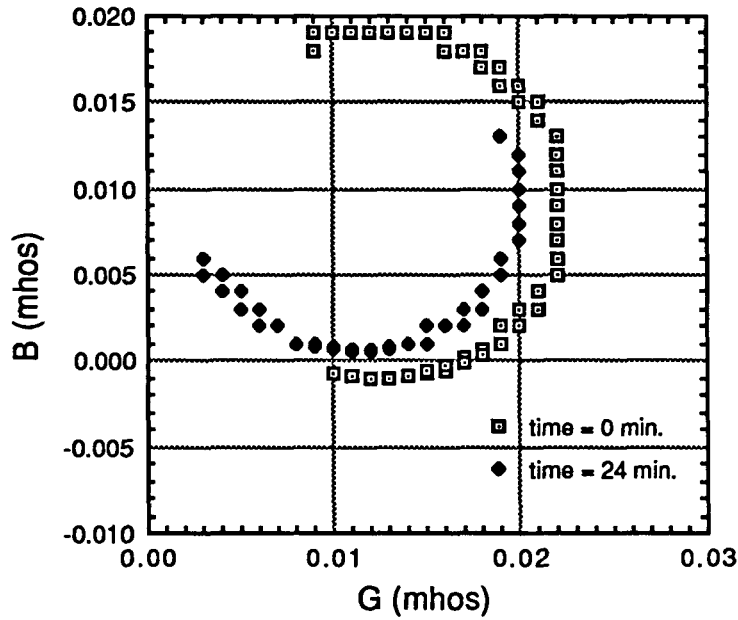


Figure 3-5. Admittance plot at time = 0 and 24 minutes for photoresist coated TFR exposed to MeOH

The effects of the series parasitic resistance and shunt capacitance can also be viewed on the Smith chart for the TFR model of Bray 18-63C K12. Figure 3-6 illustrates the effect of increasing the series parasitic resistance for values of 0, 5, and 10 ohms. As the series parasitic resistance is increased, the impedance locus of points becomes tighter and the low frequency zero-phase impedance increases or shifts in the high resistance direction as expected. Figure 3-7 shows the effect of the variation of  $C_T$  for values of 2.5, 6, and 9 pF. As the  $C_T$  increases, the impedance locus of points becomes tighter and shifts down toward the capacitive region. Equation (3.19) gives the maximum value of  $C_T$  for which the impedance locus of points contains an inductive component.

If  $C_T$  is increased any further, the impedance locus of points will be totally contained in the capacitive region of the Smith chart.

The effects of the wirebond inductance are not included since the analysis results in a circuit which would be very difficult to analyze in this fashion. However, the effects of the wirebond inductance should be included in the model for any circuit design using Libra<sup>TM</sup>. The value of this inductance is difficult to determine, however a rule of thumb for this type of inductance is 1 nH for every 0.1 inch.

### 3.3. Thin Film Coatings

In order to experimentally verify the mass loading-resonant frequency shift effect of the TFR, the electrodes were coated with thin layers of poly (methyl methacrylate) (PMMA). Initially, the electrodes were spin-coated with a uniform layer of photo-resist of nominal thickness 0.5  $\mu\text{m}$ . However, with the ALN piezoelectric thickness of approximately 5  $\mu\text{m}$ , the thin-film approximation used to derive the linear frequency shift-mass loading relations and mass sensitivity expressions were contradicted. A thin coating with a thickness of at least two orders of magnitude less than the piezoelectric thickness is necessary for accurate mass sensitivity calculations. Thus, a 2% concentration of PMMA was spin-coated onto the resonator electrode resulting in a nominal thickness of 200  $\text{\AA}$ . The zero phase resonant frequency shift due to the added thin PMMA film can easily be detected through the HP8510 network analyzer on the Smith Chart screen or by down-loading the measured S-parameters to a workstation via the HPIB and converting the S-parameters to impedance from which the zero phase frequency can be analytically determined.

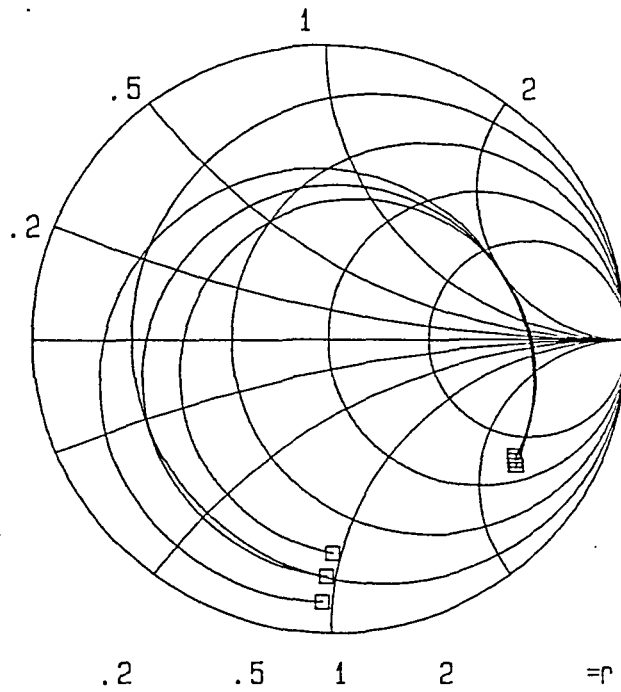


Figure 3-6. Smith chart plot:  $R_{sp} = 0, 5, \text{ and } 10 \Omega$

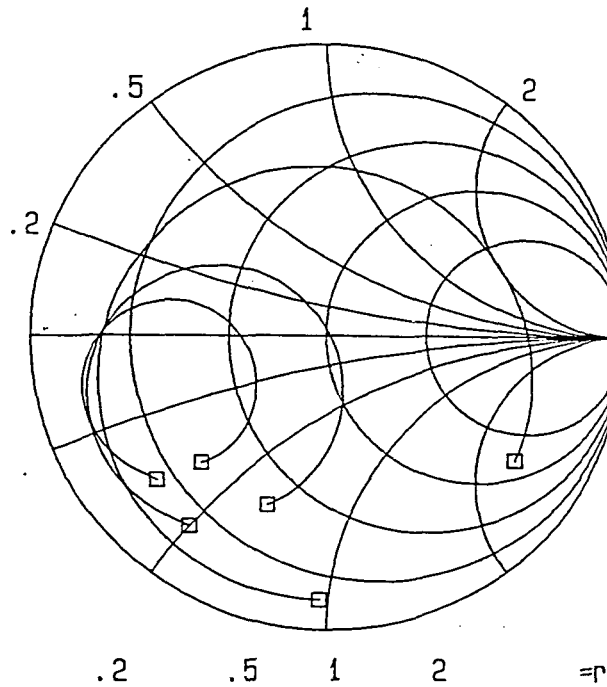


Figure 3-7. Smith chart plot:  $C_T = 2.5, 6, \text{ and } 9 \text{ pF}$

The mass sensitivity of the TFR can be experimentally found using equation (3.9). The measurable quantities are the nominal resonant frequency,  $f_0$ , and the resonant frequency shift  $\Delta f$ . The added mass per unit area,  $\Delta m$ , is calculated by measuring the thickness of the PMMA thin coating using an ellipsometer and multiplying this by the density of PMMA which is approximately  $1.2 \text{ g/cm}^3$ . The theoretical mass sensitivity can be calculated using equation (3.10) where the wavelength  $\lambda$  is twice the ALN piezoelectric thickness for fundamental mode operation. Equation (3.2) is then substituted into equation (3.10) eliminating the wavelength  $\lambda$  resulting in:

$$S_m = -\frac{2f}{v\rho} \quad (3.33)$$

This calculation neglects the added acoustic wave cavity due to the metal electrodes which is nominally  $0.25 \mu\text{m}$  thick on both sides. The density of the ALN used in this calculation is  $3.26 \text{ g/cm}^3$ . The longitudinal acoustic velocity of ALN is  $1.1 \times 10^6 \text{ cm/s}$ . Another parameter of interest which is used to characterize mass sensitivity is the minimum detectable mass (MDM). The MDM gives a more physical relation to the limit of the resonator mass sensing capabilities. The MDM is found using equation (3.34):

$$\text{MDM} = \frac{1}{S_m} \frac{\Delta f_{\min}}{f_0} \text{ S/N} \quad (3.34)$$

where  $\Delta f_{\min}/f_0$  represents the minimum normalized detectable frequency shift which is termed the normalized noise level and S/N is the signal to noise level.

To stay consistent with the existing industry standard, a normalized noise level of  $10^{-7}$  Hz/Hz is used as well as a S/N of 3. However, this normalized noise level for the TFR implies a minimum detectable frequency shift of 100 Hz for a 1 GHz resonator which is quite large. A valid argument could be made that an order of magnitude decrease in the minimum detectable frequency shift is attainable and thus the MDM value for the TFR would also decrease by an order of magnitude. Table 3-1 illustrates the mass sensitivities and MDM of the various piezoelectric devices that have been investigated and reported in various research publications. Also included in this table are the mass detection results for the TFR used in this study.

Table 3-1 illustrates the high mass sensitivity of the TFR as compared to other resonator technologies. The results from the Lewis and Lu study (16) which resulted in a mass sensitivity of 14 used quartz as the piezoelectric material. This value is the theoretical limit for quartz. The flexural plate-mode or Lamb wave oscillators reported in the White study (17) uses a  $3.0 \mu\text{m}$  thick plate of ZnO as the piezoelectric material. The resonant frequency shift of the TFR upon application of the  $200\text{\AA}$  PMMA layer varied from 1.05 to 1.35 MHz. The large resonant frequency shift is characteristic of the nominal 950 MHz resonant frequency of the TFR and thus extremely small mass changes can be detected over a relatively small area.

Table 3-1. Piezoelectric mass detection results.

Device	Experimental $S_m$ ( $\text{cm}^2\text{g}^{-1}$ )	Operating frequency (MHZ)	Calculated $S_m$ ( $\text{cm}^2\text{g}^{-1}$ )	MDM ( $\text{ng cm}^{-2}$ )
Bulk (16)	-14	6	-14	21.4
SAW(17)	-91	112	-151	3.3
Flexural plate (17)	-990	2.6	-951	0.30
Thin Film Resonator				
B18-63C M11	-630	988.6	-551.4	0.48
B18-63D J6	-613	988.65	-551.4	0.49
B18-63C J12	-574	950.95	-530.4	0.55
B18-63C J11	-514	944.5	-526.8	0.58
B18-63D H8	-469	945.3	-527.2	0.64
B18-63C H9	-463	956.65	-533.5	0.65
B18-63C H12	-445	955.15	-532.7	0.67
B18-63D L7	-440	1000.01	-557.7	0.68
B18-63D J12	-435	949.35	-529.5	0.69

## 4. TFR MASS LOADING RESULTS

### 4.1. Photoresist Thin Film Coatings

The initial proof of concept study was accomplished using photoresist as the mass detection thin film. The ease of application, selectivity of coated surface, and reactivity to common methanol were the primary reasons for using photoresist. The purpose of this study was to investigate the resonant behavior of the photoresist coated TFR as it was exposed to the methanol analyte in a sealed chamber. The desired output for this test was the resonant frequency shift as a function of the methanol exposure time, the repeatability of the resonant frequency response as a function of coatings and exposure concentrations, and the motional impedance parameter variation and resulting Q changes.

The application of the photoresist coating was done by standard spin coating and photolithographic techniques. The photoresist used in this test was AZ 1350B-SF which consisted of 2-Ethoxyethyl Acetate, Xylene, n-Butyl Acetate, Cresol Novalak resin, and Diazonaphthoquinone sulfonic Ester. Most of the proceeding components were solvents which were dissolved out during the soft bake sequence. The resulting active component which reacted with the methanol vapor was the quinone polymer. The coating thickness was nominally 0.4 $\mu$ m.

The testing sequence begins with the electrode contact of the coated TFR with the r.f. probes on the HP8510A or HP8753A network analyzer test station. The transparent gas chamber is then lowered in place to seal off the resonator surroundings. Figure 4-1 shows the TFR test system setup. Dry Argon is

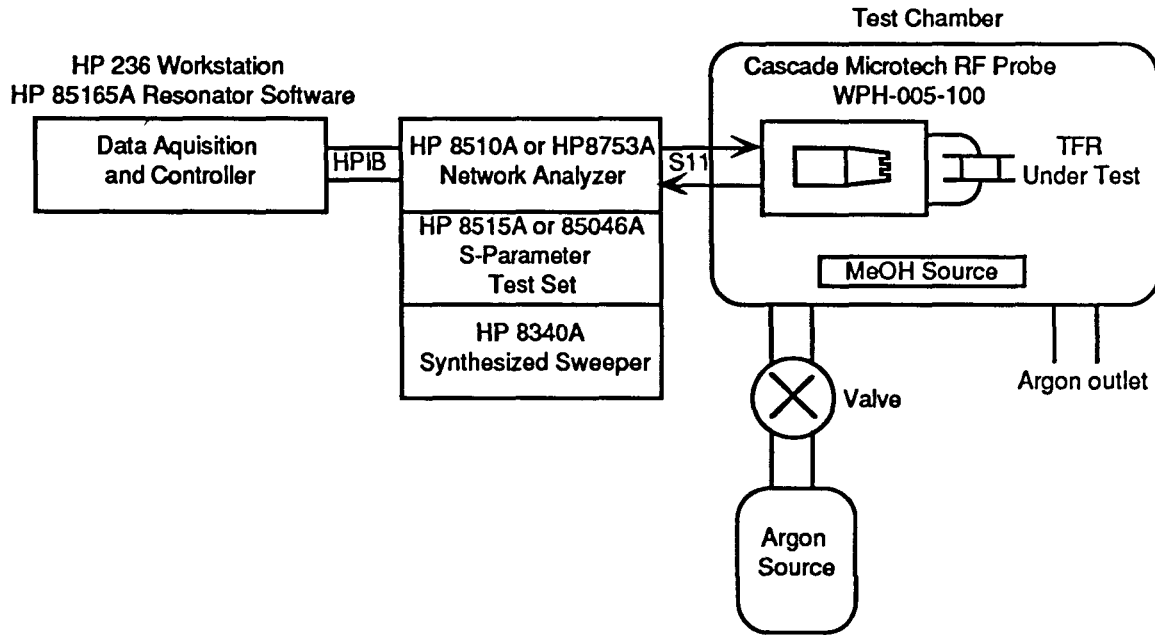


Figure 4-1. TFR test system setup

purged through the sealed chamber for 30 minutes in order to stabilize the testing environment and drive off any moisture or contaminants. The Argon purge is necessary if the effects of methanol vapor (MeOH) on the resonator coating is to be studied independent of the air moisture content. Once the purge is finished, the testing chamber is sealed off and methanol in liquid form is introduced into the resonator environment in measured amounts. The methanol is allowed to evaporate and test results are taken at set time intervals. The network analyzer measures the scattering parameters of the TFR over the calibrated bandwidth and stores the results in the HP 236 workstation connected via the HPIB interface bus. The data acquisition is accomplished using the HP85165A resonator test software which is installed on the workstation. This software will find the zero-phase resonant frequency, the series resonant frequency and calculates the motional impedance parameters,

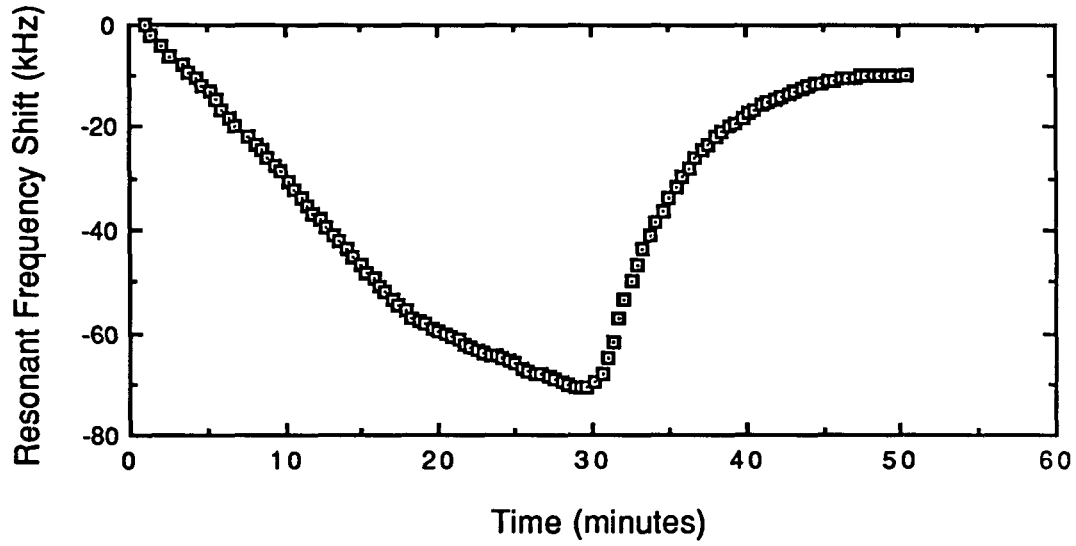
the physical parallel capacitance  $C_0$  of the resonator off resonance, and the unloaded quality factor  $Q$ . In repeatability tests, the methanol is allowed to completely evaporate and the MeOH evacuation is accomplished by purging the chamber with dry Argon during which test data is taken.

The photoresist test results begins with Figures 4-2 (a) and 4-2 (b) which illustrates the resonant frequency shift of the resonator as 1cc and 0.6cc of methanol is allowed to evaporate in the sealed chamber. After 30 minutes, the chamber is purged with dry Argon. These graphs show that the photoresist does absorb or react with the methanol vapor resulting in a negative resonant frequency shift due to mass loading as predicted by Sauerbrey or Lewis and Lu. However, the photoresist is not able to return to its initial state since the resonant frequency of the resonator remains shifted after the Argon purge and thus it has "memory". During the testing, it was discovered that after each test the most repeatable results were accomplished for which the photoresist was soft baked for 20 minutes which removed the methanol from the photoresist. An important point to make on all of the resonant frequency shift tests is that the time delay of the frequency shift is not solely due to the response delay of the resonator. In fact, the time delay is a convolution of the evaporation time of the methanol into the surrounding environment and the time it takes for the absorbant coating to accept the methanol. Thus no conclusions should be drawn on the time response of the TFR in these initial tests.

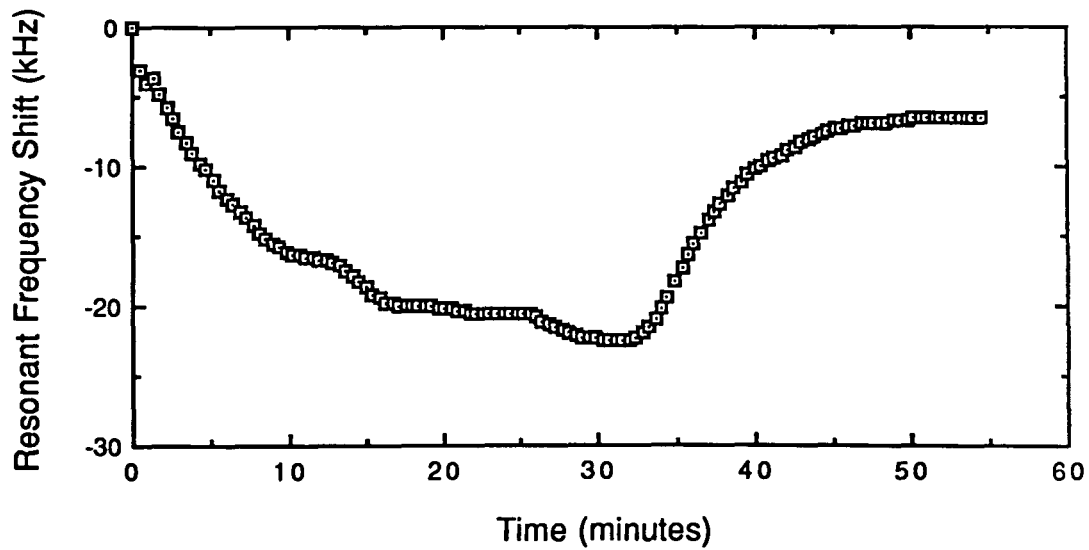
Once the negative resonant frequency shift behavior of the photoresist-coated TFR was established, more insight needed to be gained on the mechanism which was causing the frequency shift. This is accomplished by monitoring the variation of the motional parameters of the composite resonator

as the resonant frequency shifts. The motional parameters are given in equation (2.17). The motional resistance is directly proportional to the damping constant  $r$  which represents all dissipative forces; the motional resistance is also directly proportional to the cube of the thickness of the composite resonator,  $e$ , and thus thickness and energy dissipation can be observed with the variation of the motional resistance. The motional inductance is directly proportional to the density of the composite acoustic cavity,  $\rho$ , as well as to the cube of the thickness. Thus, mass loading which results in an increase in the motional inductance can be attributed to the change in density as well as the extension of the acoustic cavity. It is suspected that dominant factor which changes the motional inductance when the coated resonator is exposed to methanol is the density since the added acoustic cavity is probably very small. The motional capacitance is inversely proportional to the thickness of the acoustic cavity and to the elastic constant  $c$ . The elastic constant is related to the stiffness of the coating for which as the elasticity increases the coating will become stiffer and not deform as much for a constant applied force.

The impedance parameter variation tests for the photoresist-coated TFR was executed in the same manner as the previous resonant frequency tests except the volume of methanol exposed to the environment was considered a constant. That is, there was a large enough volume of liquid methanol in the test chamber such that it didn't completely evaporate and thus there was a source of methanol in the chamber at all times. The HP85165A resonator software was used in this test sequence to monitor the resonant frequencies and to simultaneously calculate the motional impedance parameters of the TFR under test. Each data point took approximately 2 minutes due to the data



(a)



(b)

Figure 4-2. Resonant Frequency Shift on Photoresist coated TFR  
(a) 1cc MeOH, B18-42 E11; (b) 0.6cc MeOH, B18-42 G11

acquisition and calculation.

The first data set for the photoresist-coated resonator was performed on the wafer Bray18-63b on position I15. A backside etch was performed on this wafer up to the remaining  $p^+$  membrane and thus this device was multi-moded due to the added acoustic cavity of the  $p$ -doped silicon. The metallization used to make contact on this wafer was gold since it was chemically inert to the photolithographic processing and methanol environment. Figure 4-3 illustrates a negative series resonant frequency shift of over 1000 kHz over a 20 minute span and appears to be quite linear up to 15 minutes after which the resonant frequency drops rapidly. Figures 4-4(a) and 4-4(b) are the motional impedance parameter variation versus methanol exposure time. The motional inductance increases which is characteristic of added mass while the motional capacitance decreases slightly which indicates the stiffness constant is increasing. The motional resistance increases slightly over the time interval due to added losses in the absorbant coating. The unloaded  $Q$  is shown for this time interval on Figure 4-5 which shows a decrease in  $Q$  from 1183 to 1154 and then a sharp rise at the 20 minute data point after which testing stopped due to the rapid changing frequency response of the TFR.

The second data set for the photoresist coated TFR was taken on wafer Bray18-63b position I8. The series resonant frequency variation is shown on Figure 4-6 for which a negative resonant frequency shift of 940 kHz was noted over an 18 minute methanol exposure interval. Similar trends in the motional impedance parameters are illustrated on Figures 4-8(a) and 4-8(b) as in the previous test in that the motional inductance increases, the motional capacitance decreases, and the motional resistance increases slightly.

However, Figure 4-7 shows that the Q decreases and actually rises after 12 minutes. The increase in Q was also noted in the previous test at the end of the test cycle at 20 minutes. It is not certain whether the increase in Q is correct or a function of the data manipulation process. The photoresist appears to react very actively to the methanol vapor after 12 to 16 minutes and large changes in the resonant frequency and motional parameters are noted. In fact, the onset of the resonant frequency shift from the linear to nonlinear region coincides with the region of increase in Q. The resonant frequency change is so rapid after 16 to 20 minutes that the resonant frequency data cannot converge since multiple sweeps are needed on the network analyzer for the resonator test software. Thus, large changes in the data after 12 to 14 minutes need to be carefully analyzed since there appears to higher order effects taking place which cannot be accurately accounted for.

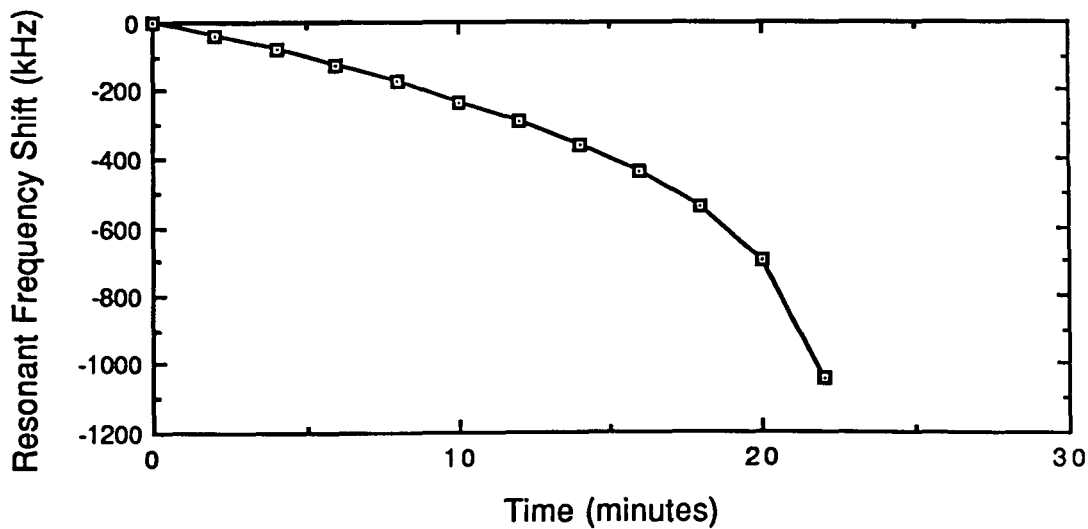
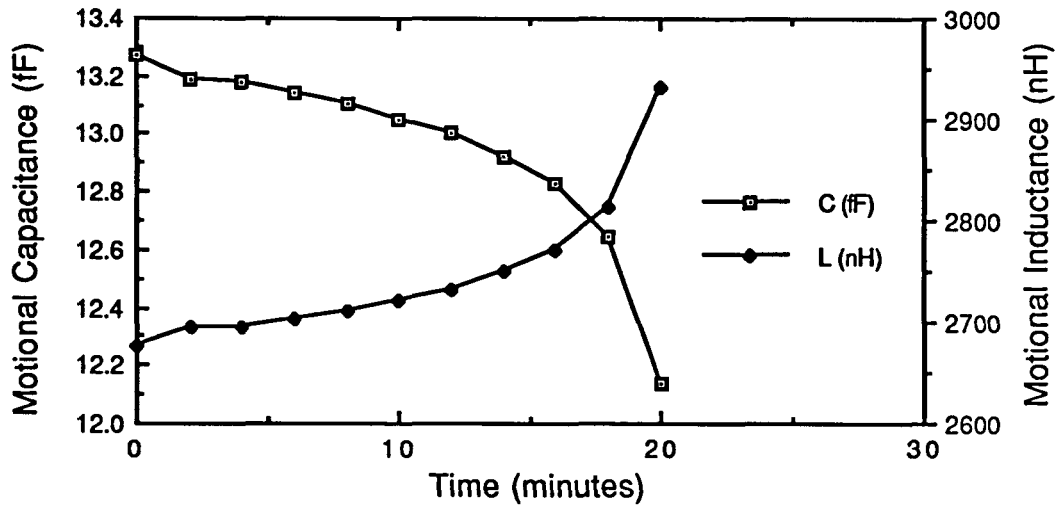
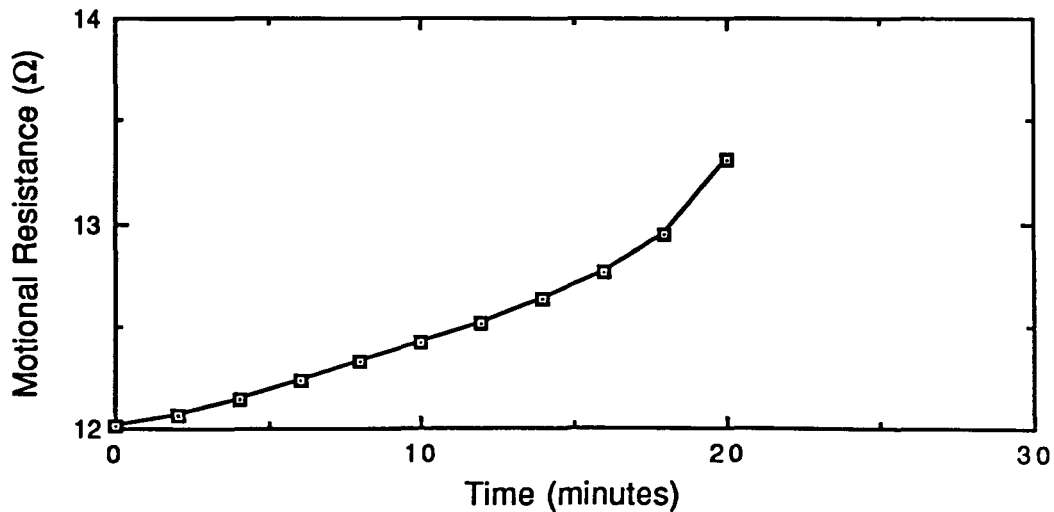


Figure 4-3. TFR series resonant frequency shift for MeOH on photoresist



(a)



(b)

Figure 4-4. TFR motional impedance parameters: (a) motional capacitance and inductance; (b) motional resistance

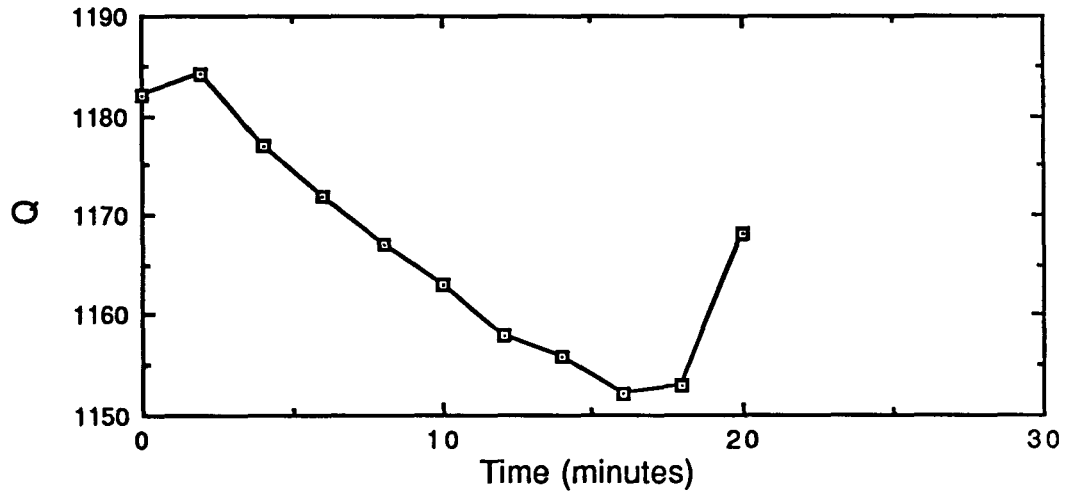


Figure 4-5. TFR Q variation

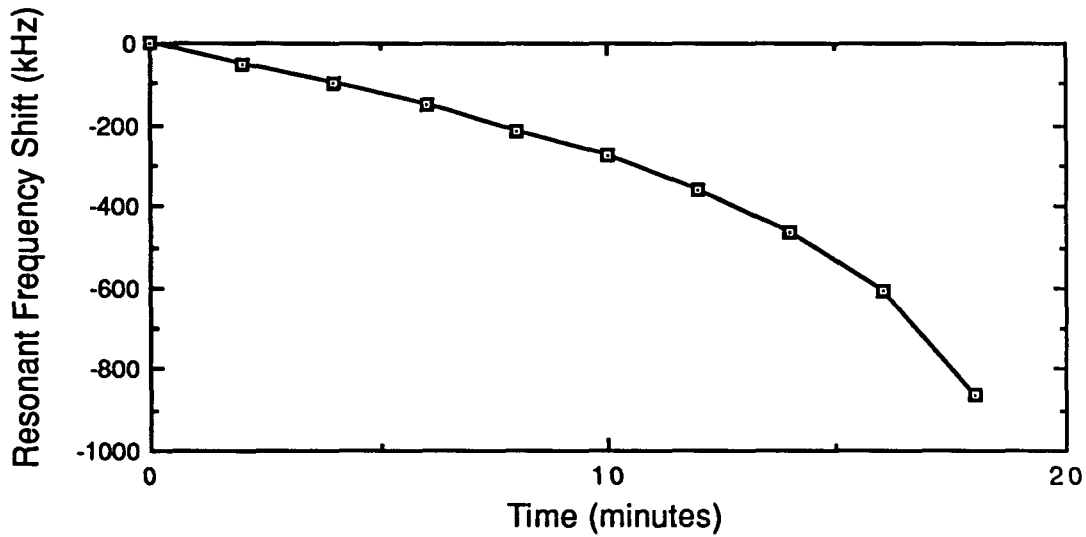


Figure 4-6. TFR series resonant frequency shift for MeOH on photoresist

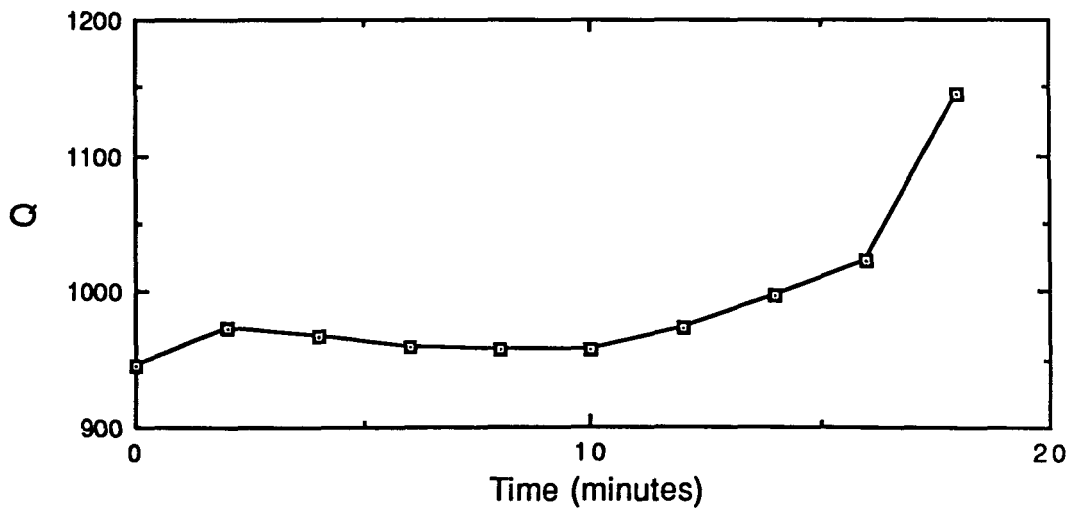
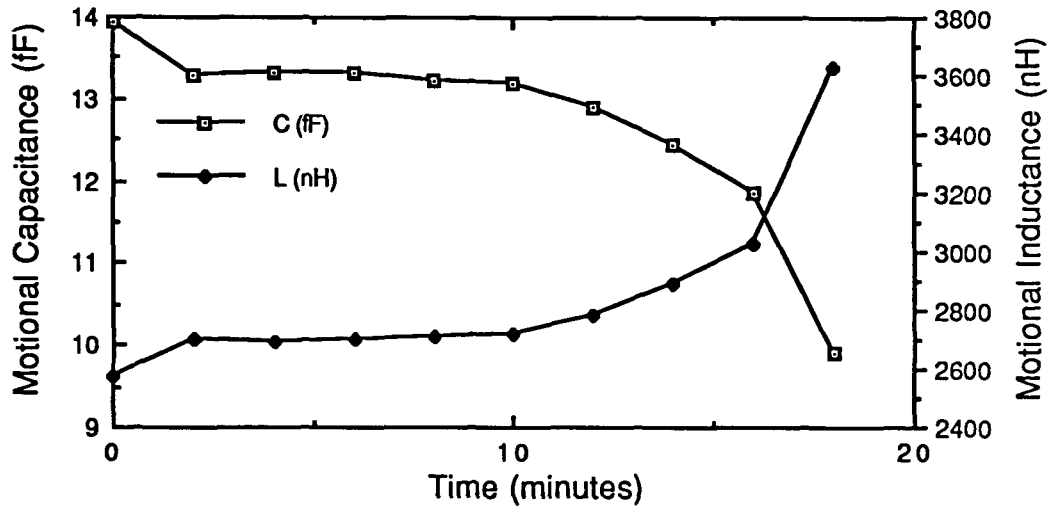
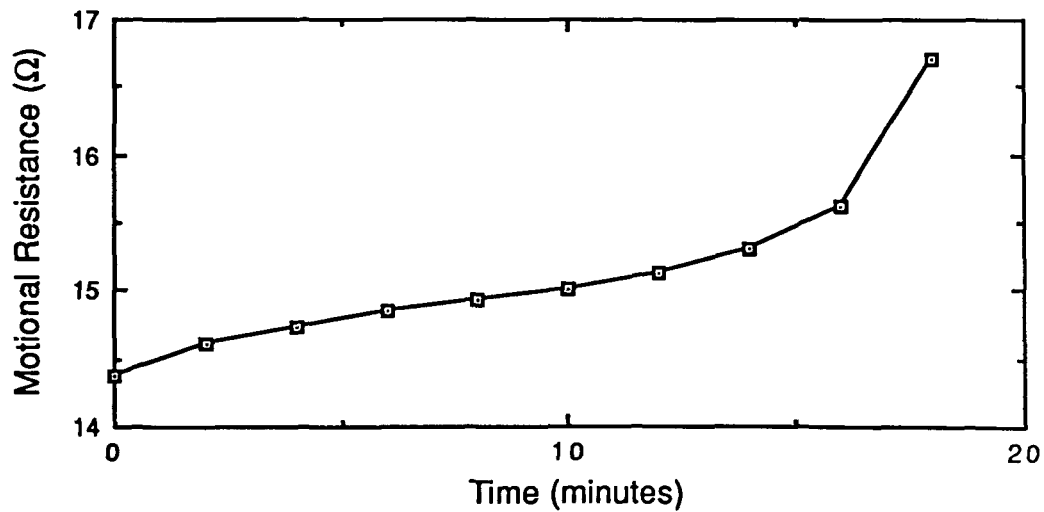


Figure 4-7. TFR Q variation



(a)



(b)

Figure 4-8. TFR motional impedance parameters: (a) motional capacitance and inductance; (b) motional resistance

#### 4.2. PMMA Thin Film Coatings

The instability and thickness of the photoresist film coatings necessitated further investigation of the resonant frequency shift and impedance parameter variation for other active thin film coatings. The coating which was chosen was PMMA since it could be applied in very thin films (200Å or less) and it was active in the presence of methanol vapor. The PMMA solution which was used in these series of tests consisted of a 2% concentration (weight/volume) of PMMA in the solvent chlorobenzene. The PMMA was spin-coated at 2500 rpm onto the entire wafer containing the TFR's and soft-baked for 30 minutes to drive off the solvent resulting in a nominal thickness of 200Å. The electrical contact was made with the rf probes by literally punching through the thin coating to get to the metal contacts. Making electrical contact through the 200Å PMMA film was not very difficult due to its relative thickness. The wafer used in this study was Bray18-63c which contained single-moded resonators and used gold as the electrode contacts. The nominal resonant frequency of the TFR's on this wafer were in the 940 to 980 MHz range.

The first test on the PMMA film was done using a constant methanol source in which the ability of the PMMA to absorb and release the methanol vapor was tested. Figure 4-9 is the result of one of the tests which shows a negative resonant frequency shift of 95 kHz over a time span of 34 minutes at which time the methanol source is removed and the chamber is purged with dry Argon. The PMMA appears to be able to release the methanol vapor rather quickly and return to its initial resonant frequency state. These results indicate that the PMMA coating will be more stable; however, since the PMMA does not

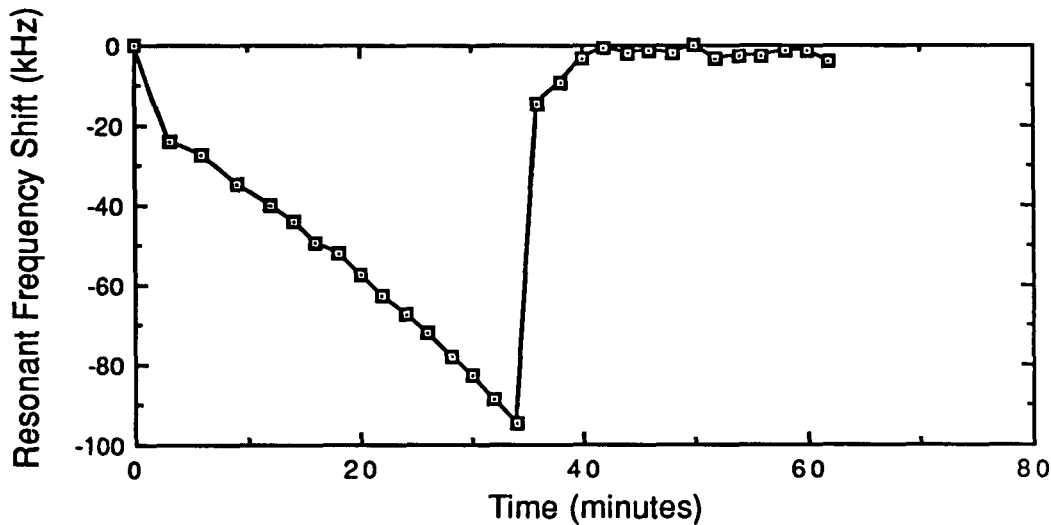


Figure 4-9. Resonant frequency shift for constant MeOH source on PMMA; Bray18-63cK12

react with the methanol vapor to the extent that the photoresist did the total resonant frequency shift will be approximately an order of magnitude less.

The resonant frequency shift in the presence of methanol vapor illustrated in Figure 4-9 proved that PMMA does have the ability to sense the methanol analyte. Thus, the next set of tests which were performed were the impedance parameter variation tests which should provide more insight to the frequency - shift effect. The first set of data taken off wafer Bray63c was at position L9. The choice of resonators to test had to be carefully done since if there were any spurs or multiple modes near the series resonant frequency the impedance results were obscure. This is due to the numerical derivative done near resonance on the reactance of the TFR to calculate the motional inductance.

Thus, a smooth resonant impedance circle was necessary if any useful data were to be taken. These tests were performed under the constant methanol source condition and test points were taken every 2 minutes if possible.

Figure 4-10 shows the series resonant frequency shift which reveals a negative relative frequency shift of 65 kHz over a 30 minute time interval. The frequency shift appears to be fairly linear over this time interval. The Q factor variation is shown on Figure 4-11 for which the Q factor actually increases from 648 to 655 at the 20 minute mark and decrease back down to 649 after 32 minutes. This change in Q represents only 1% of the nominal Q value of 648 and is fairly stable. The impedance parameter variation is shown on Figure 4-12 (a) and (b). Figure 4-12 (a) shows the motional inductance increasing which is characteristic of added mass and decreasing motional capacitance which is characteristic of increasing elasticity. The motional inductance increases most rapidly at the initial times and flattens out after 30 minutes which could indicate the PMMA is saturated and cannot absorb more methanol analyte. The motional resistance increases very slightly from 14.8 to 15  $\Omega$ 's as illustrated in Figure 4-12 (b). Evidently, the presence of the methanol analyte on the PMMA surface acts to stiffen up the coating resulting in a decrease in the capacitance which overcomes the increased loss as indicated by the increased resistance resulting in a slight overall increase in Q.

The second data set was taken at position K13. The results from this test were very similar to the previous data. The overall series resonant frequency shift was slightly greater as illustrated on Figure 4-13 with an overall shift of 79 kHz after 30 minutes. Figure 4-14 shows the Q factor remaining fairly constant over the time interval. Figure 4-15 (a) supports the theorization of added mass

and increased elasticity of the PMMA film in the presence of the methanol vapor characteristic of increasing motional inductance and decreasing motional capacitance. Figure 4-15 (b) shows a slight increase of 0.2  $\Omega$ 's in the motional resistance over the 30 minute test which is similar to the previous test.

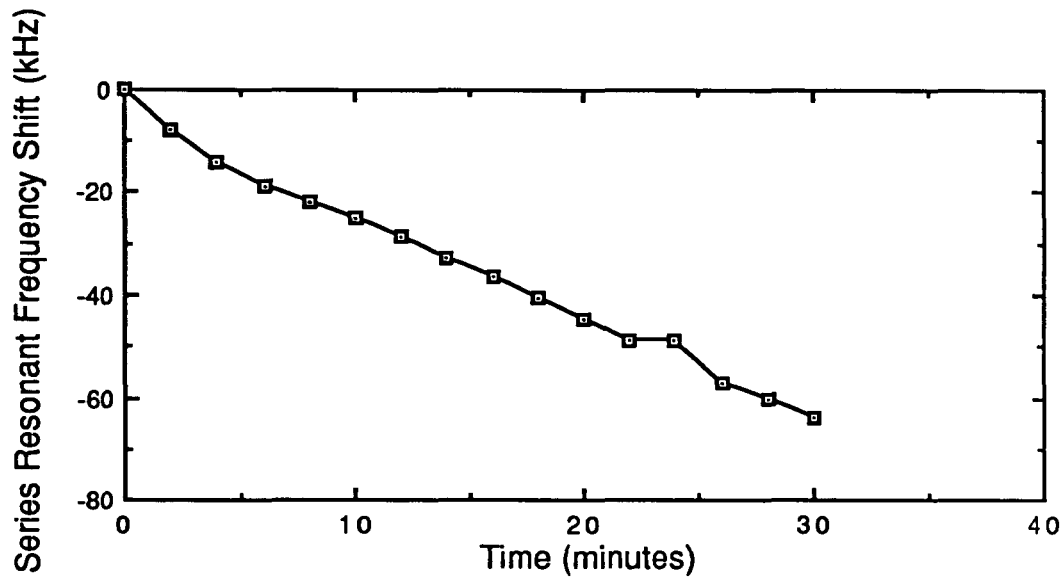


Figure 4-10. PMMA coated TFR series resonant frequency shift in the presence of methanol,  $f_s(t=0) = 972.109$  MHz

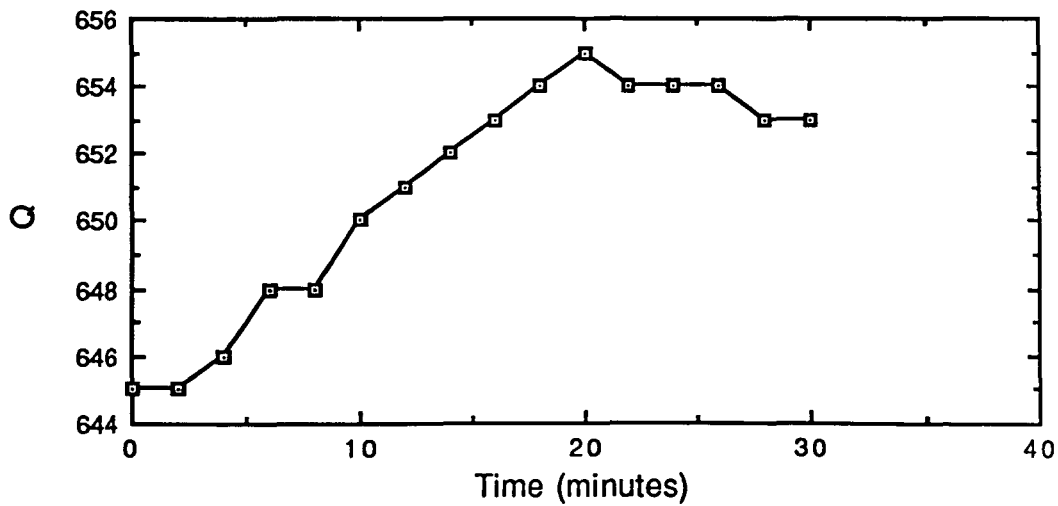
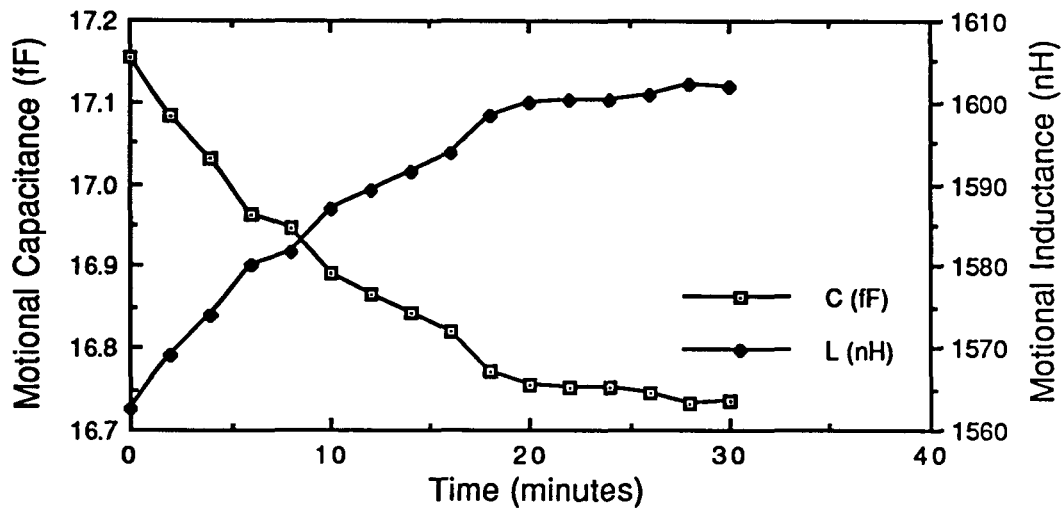
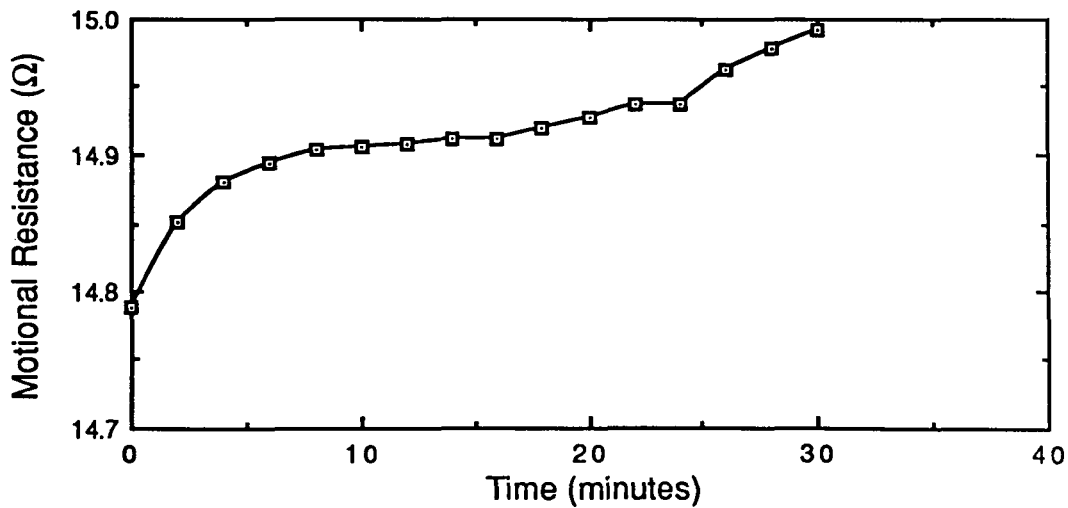


Figure 4-11. PMMA coated TFR Q variation in MeOH vapor



(a)



(b)

Figure 4-12. PMMA coated TFR impedance parameter variation: (a) motional capacitance and inductance; (b) motional resistance

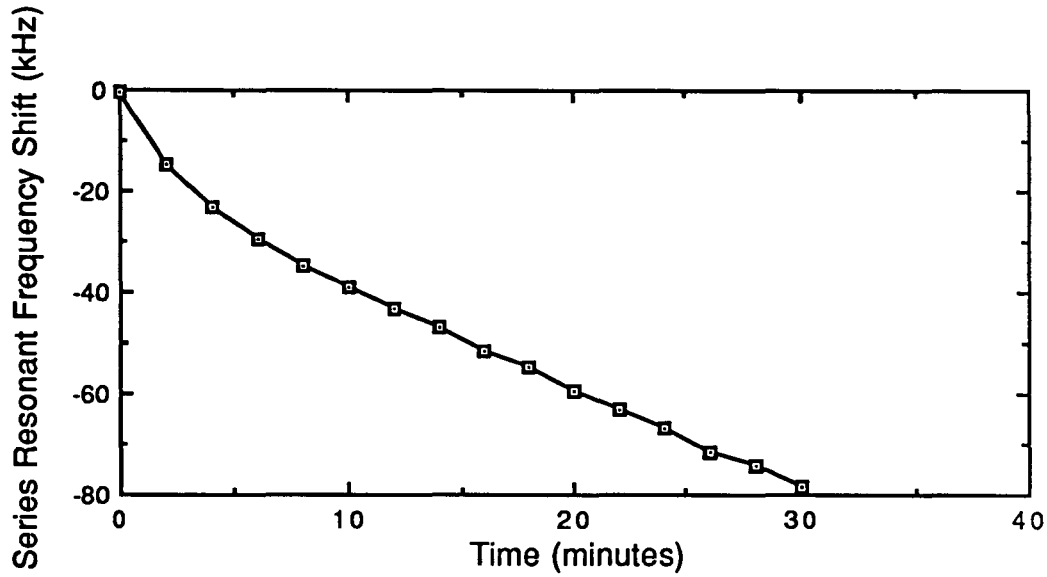


Figure 4-13. PMMA coated TFR series resonant frequency shift in MeOH vapor,  $f_s(t=0) = 972.555$  MHz

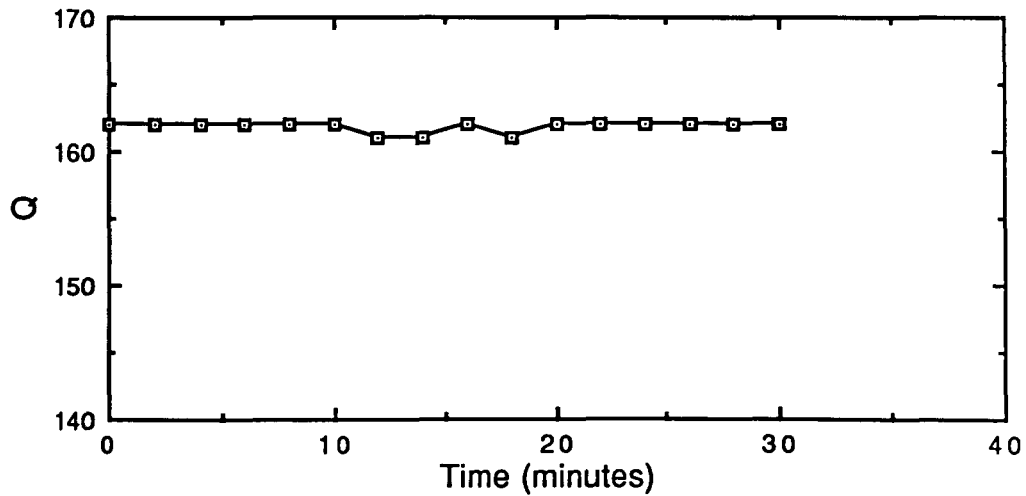
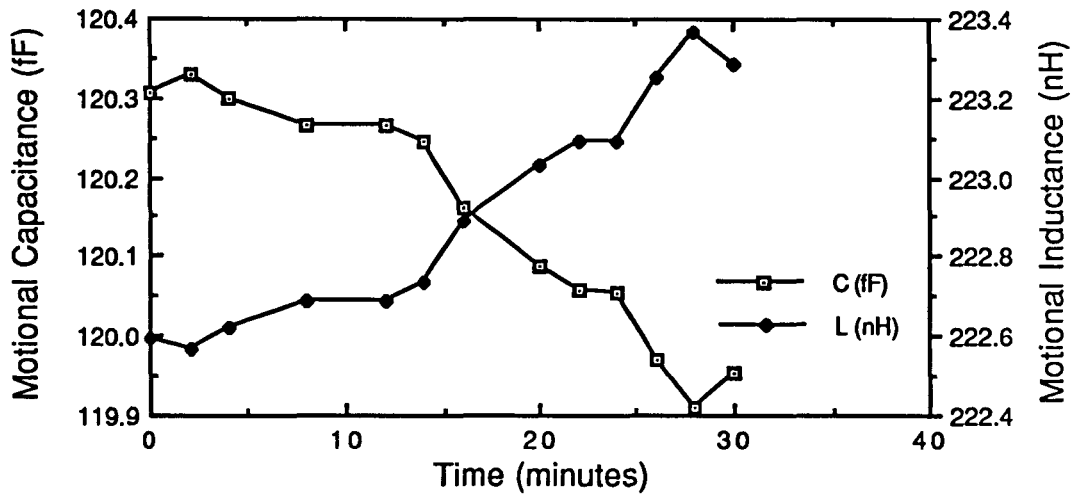
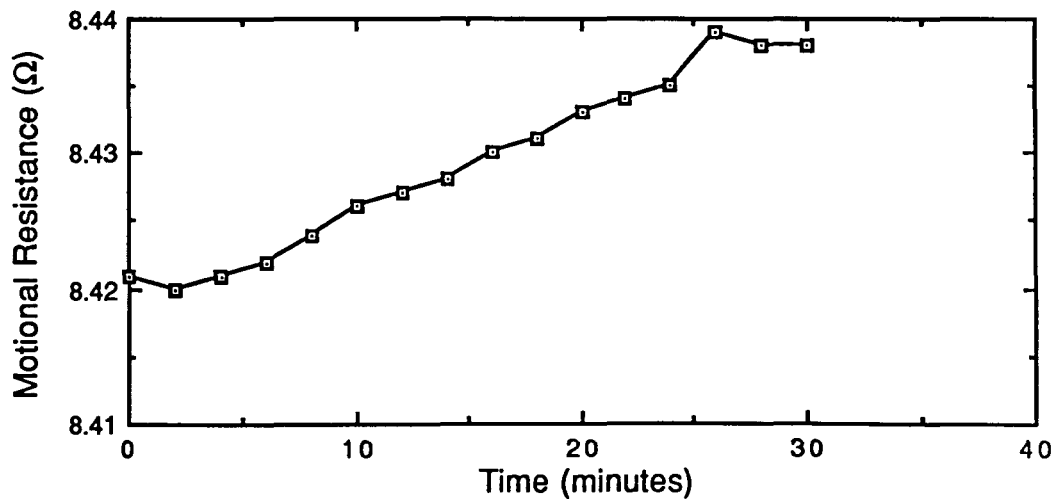


Figure 4-14. PMMA coated TFR Q variation in MeOH vapor



(a)



(b)

Figure 4-15. PMMA coated TFR impedance parameter variation: (a) motional inductance and capacitance; (b) motional resistance

## 5. SUMMARY AND RECOMMENDATIONS

The characterization and analysis of the bulk-acoustic-wave thin film resonator as a highly sensitive mass sensing device has been presented. This analysis began by investigating the operation of the TFR as an acoustic device. A one-dimensional derivation of the bulk-acoustic-wave resonator model follows which results in the motional impedance parameters expressed in terms of the dimensions, density, elastic, dielectric, and piezoelectric constants of the piezoelectric material. The equivalent circuit model of the TFR is then investigated and characterized which results in the derivation of numerous impedance points which depend on the motional impedance parameters to varying degrees. The parasitics inherent in the TFR design are presented from which the extraction of the impedance values is given.

The progression of this analysis leads to the investigation of the mass sensing characteristics of the TFR based on its acoustic and material properties. An investigation of the parasitic frequency effects of the TFR is then analyzed in order to characterize the frequency behavior due to various parasitic effects. Finally, the application of thin active coatings on the resonator electrodes allows the calculation of the mass sensitivity and impedance behavior in the presence of a gas phase analyte which proves the utility of the TFR as an extremely sensitive mass sensing device.

Recommendations for future work should first center around a complete analysis of the TFR topology and fabrication. There appears to be too many inherent parasitics with the present aluminium nitride deposition and capacitive coupling effects which degrade the frequency performance of the TFR. Once this is accomplished, a reproducible means of testing the resonators needs to

be designed since the impedance behavior of the TFR changes for each contact made with the rf probes.

A dedicated gas mixing system needs to be included in the test station. This would permit a complete analysis of the mass sensitivity of the coated TFR in terms of its resonant frequency changes and time response. The selectivity and sensitivity of various active coatings also needs to be investigated if the potential of chemical sensing is to be fulfilled.

The ultimate goal of this project is the fabrication of a complete chemical sensing system on a single silicon substrate as illustrated on figure 5-1. The mass-sensing TFR would be used as the frequency control element in an oscillator design. The fabrication of the oscillator and signal processing electronics is the next possibility from which the output of two oscillators, one coated with an active mass sensing layer and the other uncoated as a reference, could be mixed down to the audio band resulting in a difference frequency proportional to the relative frequency shift of the mass-loaded TFR.

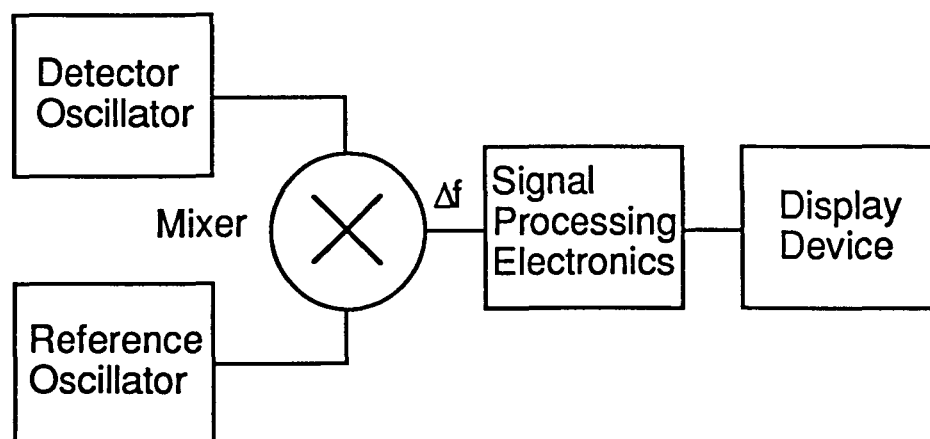


Figure 5-1. TFR chemical sensing system

**BIBLIOGRAPHY**

1. Burns, S. G., and Ketcham, R. S. "Fundamental - Mode Pierce Oscillators Utilizing BAW Resonators in the 250 - 300 MHz Range." IEEE Transactions on Microwave Theory and Techniques, MTT 32-12 (December 1984), 1668-1671.
2. Thompson, P. H., Burns, S. G., Kline, G. R., and Weber, R. J. "Design and Performance of Voltage-Controlled Oscillators Using TFR Stacked-Crystal Filters." IEEE Proceedings of the 43rd Annual Symposium on Frequency Control, May 1989, pp. 58-62.
3. Burkland, W. A., Landin, A. R., Kline, G. R., and Ketcham, R. S. "A Thin Film Bulk Acoustic Wave Resonator Controlled Oscillator on Silicon." IEEE Electron Device Letters, EDL8-11 (November 1987), 531-533.
4. Lakin, K. M., Kline, G. R., Ketcham, R. S., and Burns, S. G. "Thin-Film Resonator-Based Low Insertion Loss Filters," Proceedings of the IEEE Ultrasonics Symposium, 1986, pp. 371-375.
5. Kline, G. R., Ketcham, R. S., and Lakin, K. M. "Thin Film Microwave Acoustic Filters on GaAs." presented at the IEEE GaAs Symposium, Nashville, Tennessee, November 1988.
6. O'Toole, R. P., Burns, S. G., Shanks, H. R., D'Silva A., and Porter, M. D. "Microwave Frequency Oscillators Based on AlN: Toward Integrated Chemical Sensors." presented at Electrochemical Society Symposium, Seattle, Washington, October 1990.
7. Bottom, V. E. Introduction to Quartz Crystal Unit Design. New York: Van Nostrand Reinhold, 1982.

8. Ward, W. E., and Buttry, D. A. "In Situ Interfacial Mass Detection with Piezoelectric Transducers." Science, Vol. 249 (August 31, 1990), 1000 - 1007.
9. Sauerbrey, G. Z. Physics , 155 (1959), 223 -246.
10. Standard Methods for Measurement of the Equivalent Electrical Parameters of Quartz Crystal Units, 1 kHz to 1 GHz. EIA-512, Electronic Industries Association, April 1985.
11. Lakin, K. M., Kline, G. R., Ketcham, R. S., Landin, A. R., Burkland, W. A., McCarron, K. T., Brayman, S. D., and Burns, S. G. "Thin Film Resonator Technology." IEEE Proceedings of the 41st Annual Symposium on Frequency Control, May 1987, p. 371.
12. McCarron, K. T., Kline, G. R., Martin, J. T., and Lakin, K. M. "Growth and Characterization of Aluminium Nitride Thin Films for Piezoelectric Devices." IEEE Proceedings of the 1988 Ultrasonics Symposium, June 1988, pp 673-676.
13. Wang, J. S., and Lakin, K. M. "Sputtered AlN Films for Bulk-Acoustic-Wave Devices." IEEE Proceedings of the 1981 Ultrasonics Symposium, pp 502-505.
14. Lakin, K. M., Wang, J. S., and Landin, A. R. "Aluminium Nitride Thin Film and Composite Bulk Wave Resonators." Proceedings of the 36th Annual Symposium on Frequency Control, 1982, pp. 517-524.
15. Miller, J. G., and Bolef, D. I. "Sensitivity Enhancement by the Use of Acoustic Resonators in cw Ultrasonic Spectroscopy." Journal of Applied Physics 39, No. 10 (September 1968), 4589-4593.

16. Lu, C. C., and Lewis, O. "Investigation of Film-Thickness Determination by Oscillating Quartz Resonators with Large Mass Load." Journal of Applied Physics 43, No. 11 (November 1972), 4385-4390.
17. Wenzel, S. W. and White, R. M. "Analytic Comparison of the Sensitivities of Bulk-Wave, Surface-Wave, and Flexural Plate-Wave Ultrasonic Gravimetric Sensors." Applied Physics Letters 54, No. 20 (15 May 1989), 1976-1978.
18. King, W. H. "Piezoelectric Sorption Detector." Analytical Chemistry 36, No. 9 (August 1964), 1735-1739.
19. Crane, R. A., and Fischer, G. "Analysis of a Quartz Crystal Microbalance with Coatings of Finite Viscosity." Journal of Physics D: Applied Physics 12, (1979), 2019-2026.
20. Kanazawa, K. K. "A General Solution For the Change in Resonant Frequency of a Quartz Oscillator due to Viscoelastic Overlayers." IBM internal report, unpublished.
21. Notwozny, H., and Benes, E. "General One-Dimensional Treatment of the Layered Piezoelectric Resonator with Two Electrodes." Journal of Acoustic Society of America 82, No. 2 (August 1987), 513-521.
22. Shick, D. V., and Tiersten, H. F. "A Perturbation Calculation of the Quality Factor of the Piezoelectric Thin Film on Semiconductor Composite Resonator Resulting from Radiation into the Wafer." Journal of Applied Physics 62, No. 10 (15 November 1987), 4045-4054.
23. Adler, E. L. "Matrix Methods Applied to Acoustic Waves in Multilayers." IEEE Transactions on Ultrasonics, Ferroelectrics, and Frequency Control 37, No. 6 (November 1990), 485-490.

24. Adler, E. L. "Analysis of Anisotropic Multilayer Bulk-Acoustic-Wave Transducers." Electronics Letters, Volume 25, No. 1 (January 5, 1989), 57-59.
25. Fahmy, A. H., and Adler, E. L. "Propagation of Acoustic Surface Waves in Multilayers: A Matrix Description." Applied Physics Letters H, No. 22 (1973), 495-497.
26. Williamson, R. J. "An Improved Method for Measuring Quartz Crystal Parameters." IEEE Transactions on Ultrasonics, Ferroelectrics, and Frequency Control UFFC 34, No. 6 (November 1987), 681-689.
27. Morley, P. E., Marshall, R. J. T., and Williamson, R. J. "Crystal Parameter Measurement Using a Network/Spectrum/Impedance Analyzer." Proceedings of the International Conference on Frequency Synthesis and Control, April 1989, 6-10.
28. Hewlett Packard. Reference Manual HP 85165A Resonator Measurement Software. Hewlett Packard, Santa Rosa, CA, 1987.

## ACKNOWLEDGEMENTS

I would like to express my gratitude to my major professor Dr. Stanley Burns for his guidance and assistance in this investigation. I would also like to thank Dr. Robert Weber and Dr. Kenneth Heimes for serving on my committee.

This project, from its inception, has required the knowledge and experience of many individuals for which I am extremely fortunate to have worked with. Special thanks goes to Dr. Marc Porter and Dr. Glenn Bastiaans of the Analytic Instrumentation Center for their encouragement , support, and expertise. This project would not be possible without the help of Steve Braymen of the Microelectronics Research Center who was integral in the TFR processing. I am also indebted to Dr. Douglas Robinson and Dave Schmidt for their assistance in the processing and test station design.

I would like to thank the Department of Electrical and Computer Engineering at Iowa State University for my funding through the Harpole Fellowship. I would also like to thank the Microelectronics Research Center and the Analytic Instrumentation Center for their funding support and for the use of their facilities and equipment.

A very special thanks goes to my parents Pat and Clementine O'Toole for their inspiration and encouragement to follow my dreams.

## APPENDIX A:

**ABSTRACT: "MICROWAVE FREQUENCY OSCILLATORS  
BASED ON ALN: TOWARD INTEGRATED CHEMICAL SENSORS"**

**75-Word Abstract Form**

Extended Abstract must be submitted with the 75-Word Abstract by May 1, 1990

**Seattle, Washington—October 14-19, 1990**

Submit to: The Electrochemical Society, Inc.  
10 South Main Street, Pennington, NJ 08534-2896  
With a copy to the Organizer

**MICROWAVE FREQUENCY OSCILLATORS BASED ON  
AIN: TOWARD INTEGRATED CHEMICAL SENSORS.**

R. O'Toole<sup>a,b</sup>, S. Burns<sup>a,b</sup>, H. Shanks<sup>a,b</sup>, A. D'Silva<sup>a</sup>,  
R. Weber, and M. D. Porter<sup>a,c</sup>,

Institute for Physical Research and Technology<sup>a</sup>,  
Microelectronics Research Center<sup>b</sup>, and Department of  
Chemistry<sup>c</sup>.

The development of compact, durable analytical instrumentation is crucial for meeting the many challenges posed by emerging technology. Impetus for such development also arises from our growing environmental awareness and the related needs for new approaches for compliance monitoring.

This presentation describes the development and preliminary applications of a new class of miniaturized microbalances for the separation and quantitation of molecular species from the gas phase. These microbalances consist of organic films deposited onto ZnO or AlN piezoelectric materials as shown in Figure 1. Since these materials can be grown with small thicknesses ( $\sim 1\mu\text{m}$ ) resonant frequencies of  $\sim 100$  MHz can be achieved. Details pertaining to the construction of these devices as well as preliminary results from the quantitation of various gas phase species will be described.

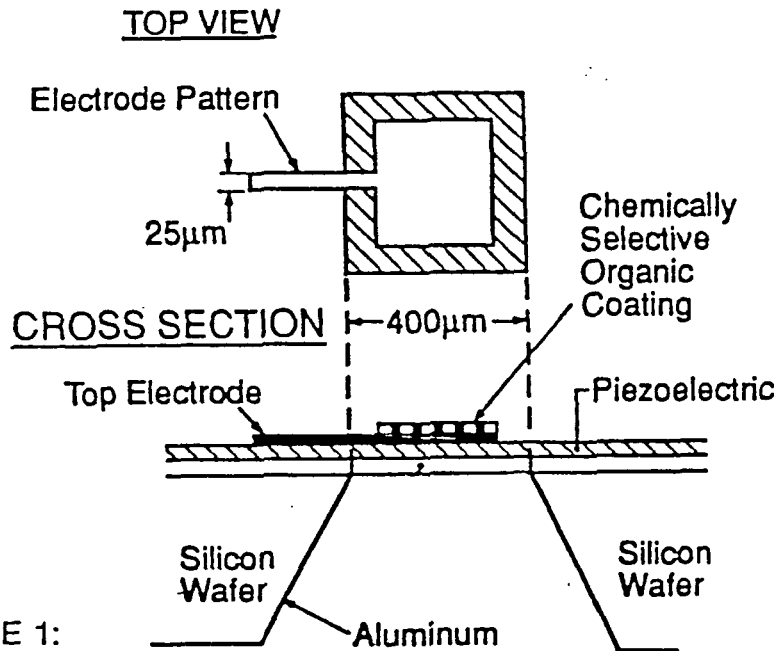


FIGURE 1:

Simplified top and cross-sectional views of an AIN or ZnO piezoelectric resonator (vertical axis not to scale). The chemically selective organic coating is shown applied to the electrode. Other deposition arrangements are possible.

**APPENDIX B:  
MAXIMUM IMPEDANCE PHASE FREQUENCY DERIVATION**

This appendix contains the detailed derivation of the maximum impedance phase frequency,  $f_{m\theta}$ , for the resonator equivalent circuit as illustrated in Figure 2-3. The impedance between the terminals A and B is found to be:

$$Z_{AB} = \frac{A1 - jB1}{C1} \quad (9.1)$$

where

$$A1 = R\left(\frac{L}{C_0} - \frac{1}{\omega^2 C C_0}\right) - \left(\frac{R}{\omega C_0}\right)\left(\omega L - \frac{1}{\omega C} - \frac{1}{\omega C_0}\right)$$

$$B1 = \left(\frac{L}{C_0} - \frac{1}{\omega^2 C C_0}\right)\left(\omega L - \frac{1}{\omega C} - \frac{1}{\omega C_0}\right) + \frac{R^2}{\omega C_0}$$

and

$$C1 = R^2 + \left(\omega L - \frac{1}{\omega C} - \frac{1}{\omega C_0}\right)^2$$

The theoretical value for the impedance phase is given by:

$$\theta = \tan^{-1}\left(\frac{B1}{A1}\right) \quad (9.2)$$

$$= \tan^{-1}\left[\frac{\left(\frac{L}{C_0} - \frac{1}{\omega^2 C C_0}\right)\left(\omega L - \frac{1}{\omega C} - \frac{1}{\omega C_0}\right) + \frac{R^2}{\omega C_0}}{R\left(\frac{L}{C_0} - \frac{1}{\omega^2 C C_0}\right) - \left(\frac{R}{\omega C_0}\right)\left(\omega L - \frac{1}{\omega C} - \frac{1}{\omega C_0}\right)}\right]$$

$$= \tan^{-1} \left[ \frac{C(\omega^2 LC - 1) - C_0(\omega^2 LC - 1)^2 - \omega^2 C^2 R^2 C_0}{\omega RC^2} \right]$$

$$= \tan^{-1} \left[ \frac{C \left( \frac{\omega^2}{\omega_s^2} - 1 \right) - C_0 \left( \frac{\omega^2}{\omega_s^2} - 1 \right)^2 - \omega^2 C^2 R^2 C_0}{\omega RC^2} \right]$$

Taking the derivative of the impedance phase with respect to  $\omega$  as defined in equation (9.2) and setting equal to zero:

$$\frac{d}{d\omega} (\tan^{-1} U) = \frac{1}{1 + U^2} \frac{dU}{d\omega} = 0 \quad (9.3)$$

where

$$U = \left[ \frac{C \left( \frac{\omega^2}{\omega_s^2} - 1 \right) - C_0 \left( \frac{\omega^2}{\omega_s^2} - 1 \right)^2 - \omega^2 C^2 R^2 C_0}{\omega RC^2} \right]$$

which when simplified results in:

$$3 \omega^4 C_0 - \omega^2 (2 C_0 \omega_s^2 + C \omega_s^2 - C^2 R^2 C_0 \omega_s^4) - \omega_s^4 (C + C_0) = 0 \quad (9.4)$$

This fourth order equation is then solved for  $\omega$  resulting in four solutions, the expression for frequency of maximum impedance phase being:

$$f_{m\theta} = \frac{1}{2\pi\sqrt{6}} \sqrt{E_2 + E_1} \quad (9.5)$$

where

$$E1 = \sqrt{12 \left(1 + \frac{C}{C_0}\right) + \left(C^2 R^2 \omega_s^2 - \frac{C}{C_0} - 2\right)^2}$$

$$E2 = 2 + \frac{C}{C_0} - C^2 R^2 \omega_s^2$$

**APPENDIX C:  
IMPEDANCE MAGNITUDE MAXIMUM AND  
MINIMUM FREQUENCY DERIVATION**

This appendix contains the detailed derivation of the impedance magnitude maximum and minimum frequencies,  $f_{\max,z}$  and  $f_{\min,z}$  respectively, for the piezoelectric resonator model illustrated in Figure 2-3. The derivation begins by finding the admittance seen between terminals A and B:

$$Y_{AB} = \frac{1}{R + jX} + j\omega C_0 \quad (10.1)$$

where

$$X = \left( \omega L - \frac{1}{\omega C} \right)$$

Equation (10.1) can be manipulated further to obtain the proper form:

$$\begin{aligned} Y_{AB} &= \frac{(R + jX)j\omega C_0 + 1}{(R + jX)} \\ &= \frac{R}{R^2 + X^2} - j \left( \frac{X}{R^2 + X^2} - \omega C_0 \right) \end{aligned} \quad (10.2)$$

The magnitude of the admittance is next calculated out:

$$|Y_{AB}| = \frac{1 - 2X\omega C_0}{(R^2 + X^2)} + \omega^2 C_0^2 \quad (10.3)$$

One of the approximations used in this analysis to simplify the order of the evaluation is that the derivative of equation (10.3) is taken with respect to  $X$  which is a function of  $\omega$  and is solved for  $X$ :

$$\frac{d|Y_{AB}|}{dX} = \frac{-2\omega C_0(R^2 + X^2) - 2X(1 - 2X\omega C_0)}{(R^2 + X^2)^2} = 0 \quad (10.4)$$

where

$$X = \frac{1 \pm \sqrt{1 + 4\omega^2 C_0^2 R^2}}{2\omega C_0} \quad (10.5)$$

The expression for  $X$  from equation (10.1) is next evaluated in terms of  $\omega$ :

$$X = \left( \omega L - \frac{1}{\omega C} \right) = \frac{\omega^2 LC - \omega_r^2 LC}{\omega C} = \frac{L(\omega + \omega_s)(\omega - \omega_s)}{\omega} \quad (10.6)$$

Since the value of  $\omega$  at which the maximum and minimum impedance occurs is very near the series resonance frequency, the sum  $\omega + \omega_s$  can be approximated by  $2\omega$  resulting in the value of  $X$ :

$$X \approx 2L(\omega - \omega_s) \quad (10.7)$$

This value of  $X$  is then substituted into equation (10.5) which can now be used to solve for  $\omega$ . However, before this is done a binomial expansion is done on the term under the square root in equation (10.5):

$$\sqrt{1 + 4\omega^2 C_0^2 R^2} \approx 1 + \frac{1}{2}(4\omega^2 C_0^2 R^2) \quad (10.8)$$

Substituting equation (10.8) into equation (10.5) and setting equal to equation (10.7) gives the equation which needs to be solved:

$$\frac{1 \pm \left[1 + \frac{1}{2}(4\omega^2 C_0^2 R^2)\right]}{2\omega C_0} = 2L(\omega - \omega_s) \quad (10.9)$$

Equation (10.9) is first evaluated using the - sign which results in the final expression for the frequency at the minimum impedance point:

$$f_{\min,z} = f_s \left( \frac{1}{1 + \frac{C_0 R^2}{2L}} \right) \quad (10.10)$$

The evaluation of equation (10.9) using the + sign results in a second order equation for  $\omega$  which is solved using the quadratic equation:

$$\omega = \frac{-2C_0 L \omega_s \pm \sqrt{4(C_0 L \omega_s)^2 - 4(C_0^2 R^2 - 2C_0 L)}}{2(C_0^2 R^2 - 2C_0 L)} \quad (10.11)$$

A binomial expansion is performed on the expression under the square root:

$$\begin{aligned} \sqrt{4(C_0 L \omega_s)^2 - 4(C_0^2 R^2 - 2C_0 L)} &\approx 2C_0 L \omega_s \left[ 1 - \frac{1}{2} \frac{C_0^2 R^2 - 2C_0 L}{(C_0 L \omega_s)^2} \right] \\ &= 2C_0 L \omega_s - \frac{C_0 R^2}{L \omega_s} + \frac{2}{\omega_s} \end{aligned} \quad (10.12)$$

Equation (10.12) is then substituted into equation (10.11). After further examination, the only frequency that can be realized from equation (10.11) is found using the - sign:

$$\omega = \frac{-2C_0L\omega_s - \left[ 2C_0L\omega_s - \frac{C_0R^2}{L\omega_s} + \frac{2}{\omega_s} \right]}{2(C_0^2R^2 - 2C_0L)} \quad (10.13)$$

Thus, the final resulting equation for the maximum impedance magnitude frequency can be found:

$$f_{\max,z} = f_s \left( \frac{4C_0L + 2CL - C_0R^2}{4C_0L - 2C_0^2R^2} \right) \quad (10.14)$$

**APPENDIX D:  
LIBRA SIMULATION FILE**

Dim

Freq GHz  
Res OH  
Ind NH  
Cap PH  
Lng mil  
Time ps  
Cond /oh  
Ang deg  
Vol V  
Cur mA

Var

Eqn

Ckt

!  
!  
!

Optimized Values for r,l,c for Bray18-63c K12

```
res 1 2 r=6.899859
cap 2 3 c=0.135461
ind 3 0 l=203.9006
cap 1 5 c=2.524755
res 5 0 r=10.00013
```

```
def1p 1 tfr1
```

!  
!  
!  
!

Measured S-parameter circuit file for  
Bray 18-63c K12

```
s1pb 3 0 tfr3
def1p 3 tfr3a
```

!  
!  
!

Optimized Values for r,l,c for Bray18-63c L12

```

res 1 2 r=8.048500
cap 2 3 c=0.164394
ind 3 0 l=163.3117
cap 1 5 c=2.840956
res 5 0 r=10.00000

```

```
def1p 1 res1
```

```

!
! Measured S-parameter circuit file for
! Bray 18-63c L12
!

```

```

s1pa 2 0 tl12
def1p 2 res2a

```

Freq

```

! Sweep .90 1.000 .001 ! Bray18-63c K12
! Sweep .968 1.009 .00068 ! Bray18-63c L12

```

Out

```

! tfr1 s11
! tfr1 mag[z1] gr2
! tfr1 ang[z1] gr1
! tfr3a s11
! tfr3a mag[z1] gr1a
! tfr3a ang[z1] gr2a
! res1 s11
! res1 mag[z1] gr2
! res1 ang[z1] gr1
! res2a s11
! res2a mag[z1] gr1a
! res2a ang[z1] gr2a

```

Grid

```

gr1 -90 90 10
gr1a -90 90
gr2 0 300 50
gr2a 0 300

```

Opt

```

! res2a model res1
! tfr1 model tfr3a

```